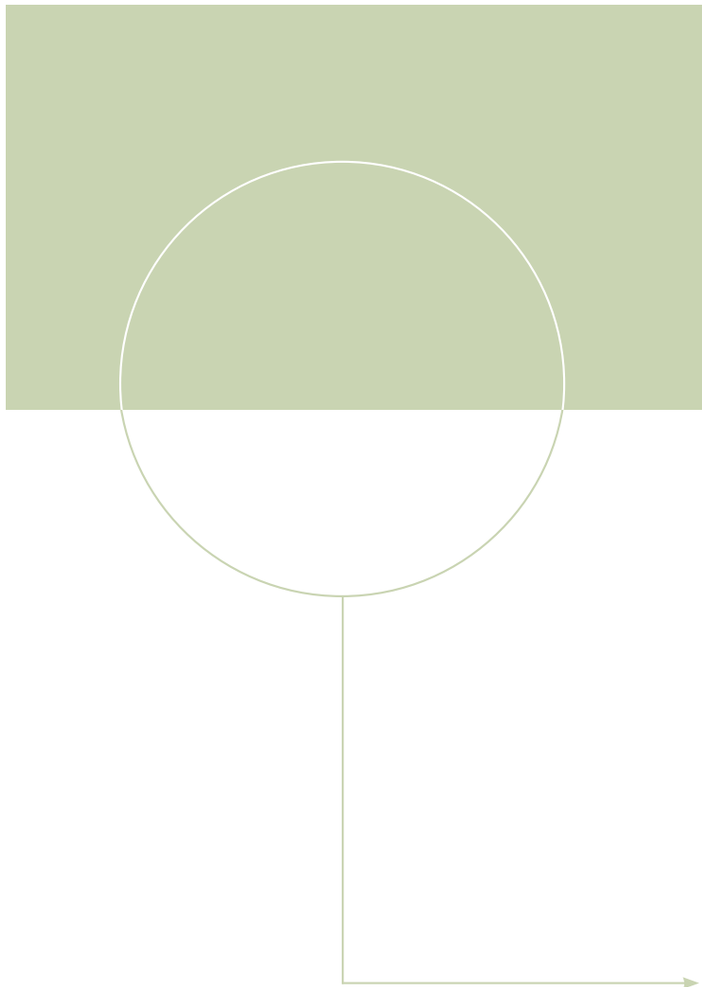

Master's thesis

2019

Jonas Klausen Espedal

NTNU
Norwegian University of
Science and Technology
Faculty of Natural Sciences
Department of Physics

Jonas Klausen Espedal

Measurements of radioactive cesium in humans; calibrating detectors using Monte Carlo simulation

December 2019

NTNU
Norwegian University of
Science and Technology

NTNU
Norwegian University of
Science and Technology

NTNU

Norwegian University of
Science and Technology

Measurements of radioactive cesium in humans; calibrating detectors using Monte Carlo simulation

Jonas Klausen Espedal

Applied Physics and Mathematics
Submission date: December 2019
Supervisor: Kathrine Røe Redalen
Co-supervisor: Lavrans Skuterud
Elisabeth Lindbo Hansen

Norwegian University of Science and Technology
Department of Physics

Abstract

The aim of this thesis is to develop a simulation framework, recreating the calibration setup that Norwegian Radiation and Nuclear Safety Authority (DSA) uses for measuring radioactivity in humans. Applying Monte Carlo simulations, this framework is used to replicate the measured calibration results. The intent is to uncover factors that may contribute to more accurate measurements.

By knowing which groups of people are most exposed, preventive measures may be taken to reduce the risk of cancer and other health issues. Due to the Chernobyl disaster, some reindeer herders are among these groups. DSA is responsible for monitoring potential radioactive contamination in Norway, and possesses a mobile laboratory where radioactivity in humans may be measured. Calibration of the detectors is performed by measuring human-shaped phantoms containing known amounts of radioactivity. The calibration setup is implemented into a framework, using the Geant4 simulation toolkit. Factors like weight, height and proximity to the detector may then be studied closely.

Virtually recreating the geometries of the calibration setup, and replicating the calibration measurements, yield information on how well the framework represents the real world. The efficiency of the simulated detector shows some systematic discrepancies from measured efficiencies, which highlight the importance of precise phantom and/or person positioning during measurements. Simulations confirm some lacking elements of the virtual setup, while simultaneously uncovering other variables, such as proximity to the detector, that have a surprisingly big effect on the measurements.

Some possible solutions, using the performed simulations and calibration data, have been suggested, but since the amount of data is limited, no clear conclusions can be drawn from this. The framework does, however, make it possible for DSA to perform further simulations and produce more calibration data, resulting in more accurate measurements.

Sammendrag

Denne oppgaven har som mål å utvikle et simuleringsverktøy, som skal gjenskape kalibreringsoppsettet som Direktoratet for Strålevern og Atomsikkerhet (DSA) bruker for å måle radioaktivitet i mennesker. Ved å bruke Monte Carlo-simuleringer, skal simuleringsverktøyet kunne reprodusere tidligere målte kalibreringsresultat. Meningen er å avdekke ulike faktorer som kan hjelpe med å forbedre slike målinger.

Ved å identifisere grupper i befolkningen som er mest utsatt for stråling, kan forebyggende tiltak iverksettes for å redusere faren for kreft og andre helseplager. Reindriftsutøvere i områdene som ble mest utsatt etter Tsjernobylulykken, er en slik gruppe. I Norge står DSA som ledende organ for å måle og forebygge radioaktivitet i uønskede områder. De har et mobilt laboratorium, plassert i en container, som inneholder utstyr for å foreta målinger av radioaktivitet i mennesker. Kalibreringen av detektorene i dette laboratoriet blir utført ved å måle menneskeformede fantomer, som inneholder en kjent menge radioaktivitet. Dette oppsettet skal implementeres i simuleringsverktøyet, ved bruk av Geant4 simulation toolkit.

Ved å gjenskape og sammenligne utførte kalibreringer med det simulerte oppsettet, kan man få informasjon om hvor nøyaktig simuleringen er. Effektiviteten i de simulerte resultatene viser systematiske feil når de sammenlignes med de målte effektivitetene, noe som understreker hvor viktig korrekt posisjonering av fantom og mennesker under målingene er. Simuleringene bekrefter noen mangler, men avdekker også faktorer som har overraskende stor betydning.

Det er gitt noen forslag til løsninger, men siden mengden simuleringer er begrenset, er det ikke nok informasjon til å bekrefte disse. Likevel viser simuleringsverktøyet at det kan brukes videre av DSA for å sørge for mer nøyaktige målinger av radioaktivitet i mennesker.

Preface

This thesis constitute the final work for my master's degree in Applied Physics at the Norwegian University of Science and Technology (NTNU). It is a thesis written in collaboration with Norwegian Radiation and Nuclear Safety Authority (DSA). The work was carried out at both Østerås, Oslo and Gløshaugen, Trondheim during the fall semester of 2019.

A big thanks to my all my supervisors, associate professor Kathrine Røe Redalen from NTNU, senior scientist Lavrans Skuterud and senior advisor Elisabeth Lindbo Hansen, for all the helpful discussions, thorough feedback and encouragement through the whole semester. Specially thanks to Elisabeth, who let me start the semester working in her office and has patiently helped me navigating Geant4.

Thanks also to the Bogdan Voaidas, for helping me setting up a simulation computer for my disposal, and Brit Wenche Meland, making it no problem for me to finish my study program one semester behind schedule.

Contents

Chapter 1

Introduction

Background

During the night leading up to 26th April 1986, one of four reactors in the nuclear power plant in Chernobyl exploded, resulting in release of massive amounts of radioactive material into the air. Material was transported long distances by wind and weather, contaminating areas far from the power plant. Today, the effects of the Chernobyl disaster is still measurable in flora and fauna in the most affected parts of Norway, with values of e.g. the isotope cesium-137, ^{137}Cs, above otherwise natural expected values (DSA (2019b)).

The explosion happened when fission of uranium got out of control, leading to an uncontrolled chain reaction, producing fission products and energy at rapid pace, too fast for the reactor to control, resulting in an explosion. One of the fission products when using uranium in a nuclear reactor is ^{137}Cs, which also is a radioactive material with a slow rate of decay. It decay by releasing energy packages containing enough energy to damage cells and tissue, thus it is desirable to limit the amount absorbed by humans (Helmer and Chechez, 2017).

During the 50s and 60s, the Norwegian Radiation and Nuclear Safety Authority (DSA) had already started to monitor radioactivity in various foods and plants, especially in the northernmost parts of Norway, due to radioactive contamination caused by testing of nuclear weapons (Wendel, 2013). When the reactor in Chernobyl exploded, the only program still ongoing, was the one where reindeer herders were monitored. Succeeding the events in Chernobyl, DSA mapped the most affected areas in Norway and started to measure both reindeer and their herders in these areas. Both these programs are still, as of 2019, ongoing leaded by DSA (DSA (2019a)).

To measure the amount of ^{137}Cs in a sample, a counting detector is used. Here, the number of energy package hitting the detector is counted, while simultaneously register the energy of the each hit. When ^{137}Cs decay, it releases most of its energy as photons at 662 keV, so by identifying the number of counted hits at this particular energy, the amount if ^{137}Cs can be predicted (Krane (1987), Lilley (2001)).

Context

DSA is the leading authority in all questions regarding radiation in Norway. They do, amongst other projects, supply information about radiation and its potential effects based upon es-

tablished research. This includes both natural doses and non-natural doses e.g. medical radiotherapy. Demand of accurate and reliable measurements is high, because of the potential effects on both personal and public health.

This thesis will look at artificial radiation, in particular radiation displaced into nature due to unfortunate events at nuclear facilities or other human-induced sources of radiation. Only ionizing radiation will be discussed, as it is what has documented effects on biological tissue.

In 2005, DSA acquired a mobile laboratory to easier perform whole-body counting in Norway, by being able to bring the lab to the contaminated areas. This laboratory, placed into a container, consists of a chair geometry setup for whole-body counting, two detector technologies and apparatus for measuring smaller samples (Skuterud et al., 2013). By geometry, a set of shapes and dimensions describing the object, is meant. Whole-body counting is a widely used method for measuring radioactivity in humans, as a means of quantifying the radioactivity present in the whole body (Fonseca et al. (2014), Krstic and Nikezic (2012)).

Assuring that a detector measures precisely what it is expected to measure, is a prerequisite for all types of measuring devices. Calibrating a detector is thus a necessary step to achieve accurate results. DSA uses a series of phantoms, called IRINA, which are built using a set of polypropylene blocks containing radiating ^{137}Cs sources with a clearly defined quantity of activity, to calibrate their systems (Kovtun and Prokofyev, 1996). Measuring these known sources of activity, the calibration results can be used to ensure that the detectors measure correctly.

The measurements performed in the laboratory are done by using detectors to record emitted photons from radioactive sources. The IRINA phantoms are built to represent people of different heights and weights. However, the range of heights and body types that can be represented are limited by the number of available blocks, as well as by time and resource constraints during calibration (Kovtun and Prokofyev, 1996). DSA had, e.g., access to the blocks for only 3 weeks in 2012, with barely enough blocks to construct the largest phantom.

Objective

In this thesis, a simulation framework will be presented to support and extend the calibration of DSA's whole-body counter with the IRINA phantom. The framework consists of a Geant4 Monte Carlo application, with a developed geometry that reproduces the container in which the detector systems are housed. Six different phantom geometries have been programmed into Geant4, and can selectively be imported into the simulation framework. The default simulations record the fluence of gamma rays resulting from decay of ^{137}Cs sources, over a simulated scoring volume. It is unknown how much, or little, differences in body size impact the measurements, thus a simulation tool could give information on questions like this.

To test the developed simulation framework, a series of simulations have been conducted. Measured data from previously performed calibration was used as comparison to test the viability of the framework.

The aim of this thesis is thus to develop a simulation framework of the calibration setup and perform a set simulations to identify the differences in measured and simulated results. This is done to let DSA continue improving their measurement routines for more accurate results.

Chapter 2

Theory

In this chapter, some theory behind the reasons why to monitor radioactivity in people as a precaution to reduce risk of cancer and promote general public health will be presented. First, a general description of the physics describing radiation and its different types will be outlined. Next, spotlighting the principles behind the two detectors technologies that DSA today uses to measure radioactivity in people and animals, and explaining how they work. The chapter then continues with some general theory of Monte Carlo simulations and how this is implemented in the Geant4 simulation toolkit. Lastly, a general look upon how and why (and the obligations) to protect against radiation.

Information about the work DSA performs, and standards and methods used by them, are provided by senior scientist at DSA, Lavrans Skuterud.

2.1 Physics of ionizing radiation and activity

In the following sections there is one book in particular that is utilized, namely Krane (1987), Introductory Nuclear Physics. This book is widely used in education for basic nuclear and particulate radiation physics. If nothing else is stated, this book is the reference through this chapter.

2.1.1 Ionizing Radiation

Radiation is a concept that can be hard to grasp without good knowledge of basic physics. The general description of radiation is transmitted or emitted packages of energy, either as electromagnetic (EM) waves or as particles, which travels through matter or vacuum.

Types of radiation

There is a distinct line for when radiation becomes a widely concern; when the radiation carries energy that is high enough to ionize. This means that the packages (particles or photons) contain enough energy to knock out an electron, removing it from an atom or molecule contained within the matter the radiation travels through. All though it is easy to state that *there is a distinct line* for ionizing radiation, the magnitude of energy required to ionize a material

varies in respect to the material it travels through. Still, radiation carrying energy over 34 eV is usually characterized as ionizing (Toxicology Data Network , 2006), as this is the average energy required to ionize air. An introduction of units used in radiation physics will be given later in this chapter.

When the energy is lower, radiation cannot ionize the material it hits, and are thus defined as non-ionizing radiation (Schwab, 2011). The easiest example of this, is to look at the electromagnetic spectrum. Here, the radiation is massless packages of energy, called photons, moving in a wavelike pattern from the source at light speed (NASA, 2013). The characteristics of EM radiation is determined by the energy, E, and frequency, ν, given from the Planck equation $E = h\nu$ (Griffiths, 1995). This means that the energy is proportional to the frequency, normalized with the Planck constant, h. At the lowest energies are radio waves (used in radio communication), slightly more energy is contained in microwaves and infrared waves, before a small slice of energies are within the visual spectrum for humans. This means visual light and all the colors. Next step at higher energies is ultraviolet, then potential ionizing x-rays and fully ionizing gamma rays (Encyclopaedia Britannica, 2019a).

Direct and indirect ionizing radiation

By taking the ways of interaction into account, ionizing radiation can be divided into two categories: direct and indirect radiation. These two categories are thoroughly described in chapter 8,9 and 10 in Krane (1987). His description goes deeply into detail in the mathematics and its implications. Just a short introduction will be given here.

Direct ionizing radiation, or particulate radiation, are particles with mass and an electrical charge. These particles can be small electrons, larger protons or heavier ions such as helium cores (α-particles) or even carbon ions. Due to their electrical charge, particulate radiation interacts with other charged particles withing the matter through Coulomb interactions.

Indirect ionizing radiation is defined as uncharged radiation and the most common are neutron and photon radiation. Since having no charge, they cannot interact through Coulomb interactions, but rather interact such that the secondary effect is causing an atom or molecule to ionize. Neutrons, for example, can be absorbed by an atom, causing the atom to release gamma radiation as a result. Photons will interact through one of three interactions explained next.

Photon interactions with matter

The photoelectric effect describes the instance when a photon interacts with an atomic electron and fully transfer its energy into the electron, making the electron energized sufficient enough to eject itself from the atom. Electrons released from an atom like this is called a photoelectron.

Compton scattering is a interaction where a photon transfer portions of its energy to an electron, causing the electron to eject itself while releasing a photon simultaneously. This second photon has less energy, and thus shorter wavelength, than the initial photon.

Pair production happens at high energies, where an incident photon have enough energy to convert into mass, when it interacts with the electric field of an atom. This creates an electron-positron pair, where all excess photon energy (all energy exceeding the rest energy

of said pair) is converted into kinetic energy, causing forward momentum for the created particles, while also recoiling the atom causing the interaction.

All of these interaction are reserved high-energy photon, characterized as X-rays or gamma radiation, which all are able to ionize the matter it travels through.

2.1.2 Energy released from a radioactive source

Alpha radiation consist of emitted alpha particles, α, which is a helium nucleus. Thus it have high energy due to its high mass of two neutrons and two protons. Taking this into consideration, the result is that alpha radiation have high damage potential, but low range, described by Krane (1987). Using different methods and detectors (some of which are presented later in this thesis), it is possible to show that a sheet of paper is enough to stop spontaneous occurring alpha radiation. However, by accelerating α particles, it is possible to penetrate deeper into a material and deposit the energy within it, causing lethal damage to cells that are hit. Among the natural occurring radioactive materials that decay through α radiation, the most notable is uranium 238, which is an isotope often used in nuclear reactors (Singal, 2015).

Beta radiation, β, is determined by some sort of conversion between electrons, neutrons and protons, thus having three different forms: negative and positive beta decay and electron capture. In negative beta decay, β^-, one neutrons is converted into a proton and an electron, $n \rightarrow p + e^-$. Positive beta decay, β^+, is the opposite, when a proton convert into a neutron and a positron, $p \rightarrow n + e^+$. The most uncommon type is electron capture, ϵ, where an electron is captured by a nucleus and interacts with a proton, creating a neutron, $p + e^- \rightarrow n$. So, for a β^- decay an electron is emitted form the nuclei, while the proton stays within the nuclei. This results in the atom changing atomic number to one higher, but keep its mass number. Likewise β^+ decay change the atomic number to one lower, also keeping the mass number. In a ϵ decay nothing is released and mass number is constant; this in not completely true as ϵ decay (and the two other decays as well) also release a relativistic neutrino, ν_e, and will leave an empty space (previously occupied by the captured electron) which can furthermore result e.g. release of γ rays. However, such in-depth look at radiation and neutrinos is beyond the scope of this thesis, but information on these topics can be found in Zuber (2015) or Fukugita and Yanagida (2003).

Gamma radiation, γ, is EM radiation with high energy. Typical wavelength of gamma radiation is 100 fm to 10^4 fm, which is (at the low end) 10^6 times shorter than visible light, thus with correspondingly higher energy (Griffiths, 1995). Compared to α radiation, γ radiation has longer reach but, singled out, smaller damage potential. Still, it is easier to produce large quantities of γ rays, therefore giving it high usage in e.g. medical radiation therapy. High energy x-rays also have the ability to ionize, dependent on the material it travels through. The distinction between γ- and x-rays is not an exact value, but usually values around 12 MeV is used. Generaly, it is the process of production which separate X- and γ-rays: X-rays is produced when electrons switch between atomic energy levels or when charged particles are decelerated in a Coulomb force field, while γ-rays is produced through nuclear decay or annihilation between positrons and electrons (Andreo et al., 2017).

In this report, the only radiation that will be looked into is ionizing radiation, specifically γ radiation. This is due to long reach and easy exposure to humans and thus potential harm to DNA and thus increased risk of cancer and other health issues (Kocurek and Woodside, 1997).

2.1.3 Units and symbols for quantifying radiation

When traveling, EM radiation behave much like a wave traveling through water, thus some of the same variables and units can be used. Wavelength, length of one cycle of the wave in the propagation direction is measured in m and given the symbol λ. At the energies given in this thesis, the wavelength will usually be in the magnitude of fm, which is 10^{-15} m. As a consequence, these also must be a time T used for one propagation (the period), measured in s, and a corresponding frequency. The frequency is defined as the reciprocal of the period, hence the unit s^{-1}. Since EM waves is described with photons, which by definition have the speed of light c (Milonni and Eberly, 2010), the frequency can also be described in terms of velocity and wavelength; $f = c/\lambda$.

As earlier stated, well described in Griffiths (1995), the Planck equation gives the relationship between energy and frequency, hence also wavelength. All though the wavelength is short, which gives high frequency, the Planck constant $h = 6.626 \cdot 10^{-34}$ Js is so small that the energy is low when measuring with standard units (Angell and Lian, 2009). Using the unit electronvolts, eV, numbers becomes more practical to use.

When measuring radiation, the rate (or frequency) of emission is measured to be the activity: $A = \mathrm{d}N/\mathrm{d}t$, with $\mathrm{d}N$ as the amount of particles released during the time $\mathrm{d}t$. In nature, there are several elements which spontaneously emits radiation, described as radioactive elements. Radioactivity, or just activity, is a measure of emissions per unit time, usually given as $[A]$ = *Becquerel* = Bq = s^{-1}. Higher Bq means higher rate for radioactive decay, thus more decay particles released per unit time.

If exposed to ionizing radiation, the absorbed dose (mainly referred to as dose) is defined as the rate if mean energy, $\mathrm{d}\bar{E}$ imparted into matter of mass $\mathrm{d}m$ (ICRP (2007)). The dose is differentiated into the absorbed dose, D_a, (the amount of radiation received by an object), the equivalent dose, $D_\mathrm{eqv} = D_\mathrm{a} \cdot W_\mathrm{R}$, (absorbed dose averaged over the whole area of organs and tissue the radiation hits) and the effective dose $D_\mathrm{eff} = D_\mathrm{eqv} \cdot W_\mathrm{T}$ (the absorbed dose including the weighted amount of sensitivity for each organ or tissue hit) (Hall and Giaccia, 2012). Here W_R is the radiation weighting factor, and W_T the tissue weighting factor. Dose is measured in Gy or Sv, which both have unit $\mathrm{J\,kg^{-1}}$. Set as standard by (ICRP (2007)), Gy is uses for the absorbed dose, while Sv is used for the equivalent and effective dose.

2.1.4 Calculating and using activity

Knowing the activity, A, is a valuable tool for quantifying the amount of a specific radioactive material present. It can also give information of age (radiocarbon dating/carbon-14 dating etc) or expected activity into the future, among many other thing. Tightly associated to A is radioactive decay and the corresponding half life, $T_{1/2}$. Radioactive decay is the action of an unstable atom (equivalent to a radioactive atom) releasing radiation, reducing the energy contained within the nucleus. This can be done through either of mentioned types of decay; α-, β- or γ-radiation. (Krane, 1987) uses this loss of energy, to introduce the half life, $t_{1/2}$. Half life quantifies the time it takes for an radioactive isotope to reach half of its original amount, meaning that half of the material has undergone radioactive decay.

Radioactive decay can be described by statistics, as it is impossible to express the exact time a specific atom will undergo decay. An expression will rather outline the expectation when a decay will occur, making the expression more reliable for larger quantities of material. By

following Krane (1987), decay is found to follow an exponential path, by expressing the decay constant, λ, as

$$\lambda = -\frac{\mathrm{d}N/\mathrm{d}t}{N}, \tag{2.1}$$

where N is the number of present nuclei and $\mathrm{d}N$ is the number of nuclei which decay in the time $\mathrm{d}t$. Integrating this expression, gives

$$N(t) = N_0 e^{-\lambda t} \tag{2.2}$$

where N_0 is the initial amount of nuclei at time $t = 0$.

Now, as half life is defined as the time it take for half of the original amount of isotope to decay, this gives

$$N(t_{1/2}) = \frac{N_0}{2} \implies \lambda = \frac{\ln 2}{t_{1/2}}. \tag{2.3}$$

This can be inserted back into (2.2), yielding

$$N(t) = N_0 \cdot 2^{-\frac{t}{t_{1/2}}}. \tag{2.4}$$

Earlier the activity, A, has been defined as the rate of which decay occur in an isotope. Mathematically this will thus be defined as

$$A(t) \equiv |\lambda N(t)| \implies A(t) = A_0 e^{-\lambda t}. \tag{2.5}$$

Finally, this makes the relation between radioactive decay, A and $t_{1/2}$ clear:

$$A(t) = A_0 \cdot 2^{-\frac{t}{t_{1/2}}}. \tag{2.6}$$

2.1.5 Cesium isotope; properties and decay

A radioactive byproduct from nuclear fission of uranium-285, is the isotope, ^{137}Cs. It is one of many byproducts, however it is one of the byproducts with medium to long half life ($T_{\text{Cs-137}} = 30.169\,\text{y}$) as opposed to other fission byproducts as $T_{\text{Ba-141}} = 18.27\,\text{min}$ and $T_{\text{Kr-92}} = 1.84\,\text{s}$ (Brookhaven National Labratory, 2019), which have significantly lower half life. ^{137}Cs was one of many isotopes that where deposited into the nature in Norway following the Chernobyl accident, but due to its half life it is still measured today. There are very few natural sources of ^{137}Cs, thus most of measured values are assumed to be traceable back to Chernobyl. Some may be result of nuclear testing following the second world war (Wendel, 2013).

Naturally, ^{137}Cs decay into a metastable state of ^{137}Ba through β^- and emits photons at energy 661.6 keV at a probability of 94.5 %. It do also disintegrates with 5.6 % probability, also by β^-, directly into the ground state of ^{137}Ba. Hence, looking for an intensity peak in an energy interval around 662 keV, will provide measurement of activity caused by Cs accumulated in the measured sample (Helmer and Chechez, 2017).

2.2 Methods for measuring radiation in humans

There exist a number of methods for measuring radioactivity, thoroughly described in Lilley (2001). Today, DSA are using two different detector technologies for measuring humans: a high purity germanium detector (HPGe) and an NaI scintillation detector. The HPGe have a narrower energy interval where is effect and are thus the best suited detector for measuring activity in a preknown energy range, such as when looking for a specifc peak in energy. However, a scintillation detector is good alternative as it measure over a larger energy spectrum. There are downsides for both; a HPGe is both expensive and inconvenient as it needs to be cooled down to low temperatures before use and a scintillation detector is more prone to surrounding noise, as it measures over said large energy interval. In the following sections the principles of each of these detector will be discussed

2.2.1 Scintillation detector

Basic principle of a scintillation detector is a crystal emitting low energy photons when exposed to ionizing gamma radiation, where the photons are energized into high energy electrons, as a result of the photoelectric effect, which are easier to detect due to having an electrical charge (Lilley, 2001). More deeply explained, the incoming gamma rays energizes the electrons in the solid crystalline, exciting them into the conducting band. When electrons then deexcite back into the valence band, photons are emitted. These low energy photons hit the photocathode at the entrance of the photomultiplier tube. This releases photoelectrons that gets both accelerated and multiplied by the dynodes into a detectable current, easily converted into a digital signal, see Figure 2.1.

When measuring ^{137}Cs, an ideal spectrum would be a single full-energy peak at $E_p = 662\,\text{keV}$ (Helmer and Chechez (2017)) and nothing else. This is not a realistic approach, however, as the radiation does not transmit all its energy to the scintillation crystal.

The full-energy peak corresponds to γ rays transferring all its energy, E_p, to the crystal. This can happen through one or several interactions. If it happens over several interactions, these repeatedly scattered γ rays will for each interaction deposit a smaller amount of energy along their paths, thus creating a continuum of lower energy photons that generates corresponding low energy photoelectrons. Hence, it is expected to measure counts at lower energies, called the Compton continuum. The highest energy of this plateau, called the Compton edge, is given by maximum possible energy transfer in a Compton scattering, which is when the incoming particle is scattered backwards.

2.2.2 Semiconductor detector

A way to explain semiconductor detectors, is that incoming radiation excite electrons from the valence band into the conducting band. Then it create an electric pulse that is detectable and proportional to the energy deposited into the semiconductor. In other words, the detector works as a normal semiconductor, but instead of using an electric input (as in electrical devices) it uses the incoming radiation energy to energize the electrons in the valence band.

Briefly, a semiconductor works by having a band gap of a certain width where the electrons may spontaneously (though rarely) jump across the gap into the conduction band, having a hole/vacancy (absent of electron) jump the other way (Lilley, 2001). With enough exchanges

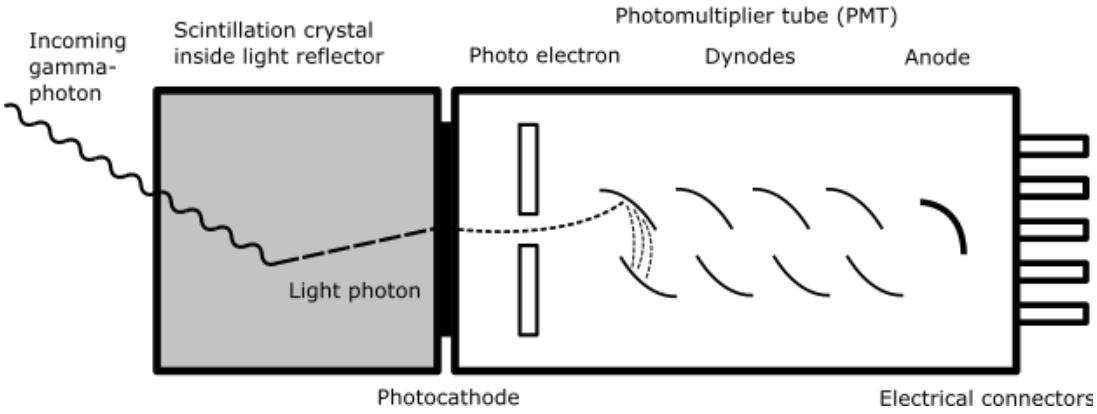

Figure 2.1: A scintillation detector, where incoming γ radiation produces light photons while interacting with the NaI(Ti) crystal. In the PMT the photons, due to the photoelectric effect, produces photoelectrons, that are mulitplied into the current which the electrical connector detects. Drawing inspired by Lilley (2001).

of electrons and holes, a current is created and the before near-insulating material is now a conductor. A second input signal is able to adjust the current.

To achieve a reliable output signal for a semiconductor detector, the probability of an electron spontaneously exciting across the band gap needs to be as low as possible, preferable nil. The semiconductor is therefore cooled down to 77 K (by liquid nitrogen) so that the electrons have next to no excess thermal energy to make the jump (Lilley, 2001).

Semiconductor detectors functions in two different ways, where the main principle is still the same: p-n junction detectors and intrinsic detectors. A p-n detector use a sandwich of usually doped silicon (Si) to increase the amount of holes (positively charged (p-doped)) or the amount of electrons (negatively charged (n-doped)) (Krane, 1987). As this is how most semiconductors are made, this technology is well-known and relatively cheap. An intrinsic (also called hyperpure) detector is made by a single crystal, usually of Germanium (Ge), that have n- and p-doped contact on each side for the crystal to enhance the functionality. As both Ge and Si is located in group 14 in the periodic table, they share a large amount of the same characteristics. The sole reason that Ge is preferred over Si in intrinsic detectors is due to its higher atomic number, Z. Higher Z makes Ge more efficient stopping incoming γ rays, hence improve the efficiency of the detector (Lilley, 2001). A simplification of an intrinsic detector is show in Figure 2.2.

2.3 Simulating radiation

2.3.1 Basics of Monte Carlo simulation

From Merriam-Webster's collegiate dictionary (2019) the concept of simulations is defined as "the imitative representation of the functioning of one system or process by means of the functioning of another". Though this is followed by an example of usage (which includes a formulation using "computer simulation"), one might argue that this rather simple definition also defines the whole academic area of physics; taking one existing thing from the physical world and describe it in means of math and equations. Today, more and more advanced tools are developed to mimic natural systems, most efficiently by using computational power from computers and software. One of the most used simulation concept today

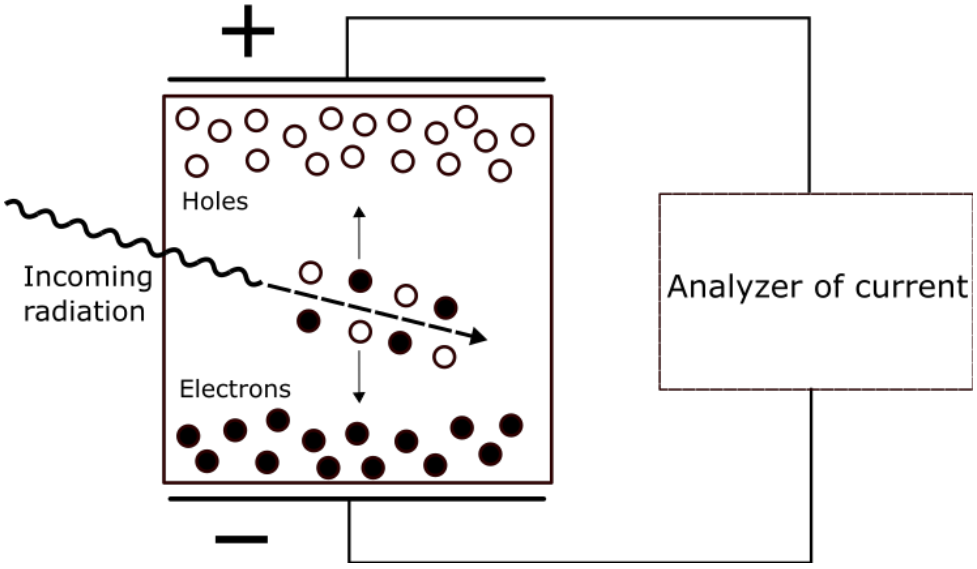

Figure 2.2: A concept drawing of a semiconductor detector. Incoming γ radiation energize electrons within the Germanium crystal, causing electrons to be free and transferable and thus able to create a detectable current.

is Monte Carlo (MC).

While there is no exact definition - nor one single method (Harrison (2010)) - of MC, the concept throughout is still the same. As the name is inspired from the Monte Carlo Casino is Monaco, it indicates that some sort of randomness is included. Fundamental for MC is that there are some probability density functions (PDFs), which define the different possible outcomes and their respective probability to each step of the interaction. From these functions, one repeatedly sample by feeding random numbers into the inverse cumulative distribution functions (CDF), which will output sets of random numbers satisfying the PDFs. A CDF gives the probability that a sampled number from the PDF is less than or equal to the input; the PDF display the probability, $p(x)$, that a variate has value x, while the CDF display the probability, $P(x)$, that a variate has value $\leq x$. The CDF is given by the fundamental theorem of calculus, $P(x_0) = \int_a^{x_0} p(x)dx$, where a is the lowest limit of where x is defined (Adams and Essex (2013)).

In MC simulation of radiation physics, one usually would like to examine the path of photons, electron or other particles into matter. For photon- or particle-emitting sources, the concept is to let the surface or object transmit the radiation at a given energy in any direction desired and calculate each track/path. The photons or particles interact with the matter either through scattering or absorption. Whichever of these interaction that happens, is determined probabilistic, highly dependent on the matter cross sections. Thus, determine the density and characteristics of the matter is especially important.

The *mean free path*, which is the average length of a photon track before it interacts, is given as $1/n\sigma$, where n is the number density of a target medium with cross section σ. Now, the probability that a photon either scatter or get absorbed within the length $\mathrm{d}l$, is therefore $n\sigma\mathrm{d}l$. Following this, the probability of the photon *not* interacting is $1 - n\sigma\mathrm{d}l$. Looking at the probability of a photon traveling the distance L into the medium, one needs to divide L into N equally slices of equal length and let $N \to \infty$:

$$P(L) = \left(1 - \frac{n\sigma L}{N}\right)^N = e^{-n\sigma L} = e^{-\tau} = P(\tau), \tag{2.7}$$

where $\tau = n\sigma L$ is called the optical depth.

While this gives the distribution of depth into the matter, the angular distribution for the scattered photons is given by the probability of a photon changing direction as it scatters, $P(\cos\phi)$, with ϕ as the scattering angle. This can be done using several different phase function, usually Compton scattering (Wood et al. (2013), Frisvad (2011), Forgan (2009)).

2.3.2 Geant4 simulation toolkit

Geant4 is a powerful toolkit that let the user define particles and materials and simulating the particles passage through the given geometry (Agostinelli et al. (2003), Allison et al. (2006), Allison et al. (2016)). Since the initial release in 1998, the toolkit have undergone huge improvements and is still a reliable tool for simulating particles interacting with matter. Among other, the toolkit can simulate energies over a wide spectrum, from a couple eV up to several TeV and have integrated support for the National Institute of Standards and Technology databases, containing information on materials and elements. It does also have a functional method for converting 2D and 3D Computer Aided Design files (CAD) into geometries within the toolkit. The toolkit allows complex geometries implemented through C++. It uses multithreading as a method of undertake big simulations as efficiently as possible. The software is used for several applications; electromagnetism, high energy physics, medical and radiation, astrophysics, space engineering etc.

This study shows a small part of the capabilities of Geant4, where the geometry of the experimental setup is rather simple, described in section 3.1. While there are ways to improve the simulations, this would require more knowledge of the program. Here, the particles are simulated in complete tracks, from its origin propagating outwards at a pre-decided distribution from the chosen source. The tracks are calculated through the matter it travels and are then scored at a given confined volume within the defined world. Hence, more calculations than necessarily are executed, as there are just a fraction of the calculated track which hit the scoring volume.

2.4 Radiation protection

International Atomic Energy Agency (IAEA) and International Commission on Radiological Protction (ICRP) are two international organization that administers radiation protection with slightly different focus. IAEA is an suborganization of United Nations (UN) that work for safe, secure and peaceful usage of nuclear technology and industry. ICRP handles issues directed towards protection of ionizing radiation, both for the general public, for personnel working in a profession where ionizing radiation need to be handled and other situations where ionizing radiation occurs, such as medical treatment.

In ICRP (2007), exposure situations are divided into planned, emergency and existing exposure. Occupational exposure and planned medical treatment are examples of planned exposure, where it is possible to make precautions to minimize its magnitude and extent. An emergency exposure is an unplanned, and in most cases unwanted, exposure which might be a consequence of a nuclear event, resulting in a leak of radiation to the surroundings.

Lastly, existing exposure is exposure that already exist of which protective countermeasures can (or should) be made; radioactive material present in nature as an example.

Following sections will present guidelines for radiation protection in Norway as well as theory behind different techniques of measure radiation and elucidate the topic of why to monitor radioactivity.

2.4.1 Protecting against ionizing radiation

One of the main goal of radiation protection is, as stated by ICRP (2018), NCRP (2019) and Hall and Giaccia (2012), is to "limit the risk of stochastic effects". This means to limit the amount of radiation received by a populatio, to reduce the risk of cancer and other heritable effects. Figure 2.3 shows the relative estimated relationship between exposed dose, to the probability of being effected in some way. While the deterministic effects, that is the effect that have been tested and determined, have a clear threshold to where the effects occur the stochastic (or random) effects always have probability to occur. Thus, the goal for radiation protection is not only to reduce the amount of exposed radiation below the deterministic threshold, but ever below such that the stochastic effects also are minimized.

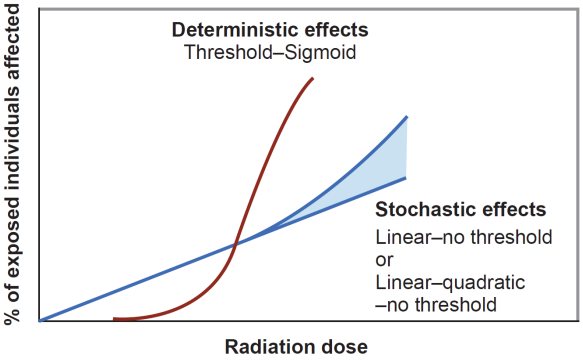

Figure 2.3: Occurrence of deterministic and stochastic effects as a function of radiation dose. Figure taken from Hall and Giaccia (2012), page 259.

Briefly mentioned in section 2.1.2, the different types of ionizing radiation have different range. Both α and β have short range, with α having the shortest. This means that small amount of matter is needed to stop emission of these kinds. Krane (1987) describes the mathematics of penetration depth well. If humans are to be harmed by these types of radiation, they need (in most cases) to make it into the body through the digestive or respiratory system, i.e. internal exposure (Komperød et al., 2013). When examine external exposure, the more penetrating γ radiation is the dominant factor that here will be taken into account. However, if dose and/or proximity to the radiating source high, α and β also need to be accounted for. To stop a beam of α particles, a sheet of paper will stop the majority, while a 2 mm to 4 mm thick plate of aluminium will stop most β radiation (QST, 2019). To stop γ radiation, a similar set value cannot be given as the long wavelength gives γ rays long penetration depth, but due to properties of lead, Pb, a slab $>$ 5 cm will stop most mid-energy γ rays (Encyclopaedia Britannica, 2019b). Notably, material consisting of elements with high atomic numbers yields best γ protection. Higher energy γ radiation will however need material with higher stopping power for protection, alternatively higher thickness of a material with lower stopping power.

Beside this, there are four major factors of radiation protection: time, distance, shielding and contamination (Eaton and Schneider, 2014). To achieve best protection against radiation, the time of exposure must be low, the distance to the source high, the shielding between the object and the source as good as possible and the possibility of radiation contamination (leakage to the environment) as low as possible. Detailed review of radiation protection can be found in the reports by the ICRP, which covers in-depth reviews of planned exposure,

emergency exposure, medical procedures, medical staff etc. ICRP (2007) and ICRP (2018) are among the reports most used for this thesis.

2.4.2 National and international guidelines

In Norway, the work of following up ICRP standards relating radiation protecting and limitation of irradiation is done by Ministry of Health and Care Services and formulated in the Law of Radiation Protection and Use of Radiation (Stålevernsloven) (Helse- og omsorgsdepartementet, 2019b). The main purpose is to prevent potential harm to human health and contribute to conservation of the environment.

The law is followed by The Act and Regulations on Radiation Protection and Use of Radiation, which gives thoroughly guidelines and rules for management of the law (Helse- og omsorgsdepartementet (2019a)). In the same scope as the law, the regulation objective is to secure safe usage of radiation and radiating material, as well as preempt damage to human health and preserve surrounding environment.

DSA is the national expertise and authority that manage all questions regarding safety and security within Norway, but do also international duties (Harbitz (2019)).

Internationally DSA works together with, and on behalf of, the United Nation specialized agency IAEA, the European Union and ICRP. Through these forums DSA and the other member countries, specialized agencies works together to promote safe, secure and peaceful use of nuclear technology, as well as standardized security routines and recommended treatment of nuclear waste, radiation and transportation.

2.4.3 Guidelines for radioactivity in food and population

ICRP use the linear no threshold (LNT) model as basis for radiation protection. This model predicts that if the dose is doubled, the risk of harm is doubled. When the LNT model spotlight the known stochastic effects, the conclusion is that there does not exist a safe limit of dose where radiation does not have effects on human health. Therefore, the ALARA (As Low As Reasonably Achievable) principle is widely used both for medical radiation and public radiation security (Edwards and Hendee, 1986). It encourage to minimize the total dose to a level that is neither too intervening to a normal life nor too costly of achieve. Thus, there are standards to which amount of ionizing radiation human and food might contain or imbibe before counteractions are to be made.

The Norwegian Food Safety Authority has set, in collaboration with DSA, restriction for activity per weight in food, measured in $\mathrm{Bq\,kg^{-1}}$. International recommendations has set limitations of absorbed dose to humans, giving rise to national recommendations of activity in different kinds of food, based upon nutrition sources in a country. Generally, these recommendations are relatively alike in most countries. In Norway there are some exceptions; domesticated reindeer, game and wildlife and freshwater fish. This is due to the fact that these exceptions are not classified as basic wares used in everyday

Table 2.1: Limit for radioactivity for food in Norway à 2017 (Komperød et al. (2017)). The exceptions are domesticated reindeer, game and wildlife and freshwater fish.

Product	Limit, $\mathrm{Bq\,kg^{-1}}$
Milk and baby food	370
Exceptions	3000
Other	600

cooking and they have cultural significance. Domesticated reindeer specifically is important for the Sámi population in the Nordic countries, both culturally and economically. See Table 2.1 for the given limits.

There does also exist some more restricted recommendations for pregnant, breastfeeding woman and small kids, limits that are aimed towards how much radioactivity that could be consumed during one year.

2.4.4 Chernobyl and nuclear testing

Following the incident at Chernobyl in 1986, a substantial amount of the radioactive ^{137}Cs isotope was deposited over parts of Norway as a consequence of wind and rain. In Figure 2.4a the areas that were most effected is displayed. The radioactive material that was spread was stored in the soil and especially in mushrooms and lichen, both of which are important sources of nutrition for reindeer and other wildlife. Due to international recommendations Norwegian authorities had risen the limit of radiation to 5 mSv as effective dose for humans in 1986, but were lowered to 1 mSv for the years after. According to ICRP (1975) a dose of 1 mSv is estimated to equal a whole-body ^{137}Cs concentration of 400 Bq kg^{-1}. So, it was reasonably to start applying countermeasures when the activity was close to or above this limit.

Among the most effected groups are the reindeer herders, whom consume more reindeer meat than an average person, and thus this group have been monitored until today, visualized in Figure 2.4b Since the mid 90s the average among the herders have been below 400 Bq kg^{-1} and sinking as expected (Mehli et al. (2000), Skuterud and Thørring (2012)). Still, the herders have been regularly measured such that a complete set of data is produced.

Another source of radioactive contamination into Norway can be traced back to nuclear testing facilities, both for energy and for nuclear weapons, in the period after World War II (Wendel et al. (2013), Wendel (2013)). This source have deposited slightly heavier particles, majorly different uranium and plutonium isotopes, in the nature.

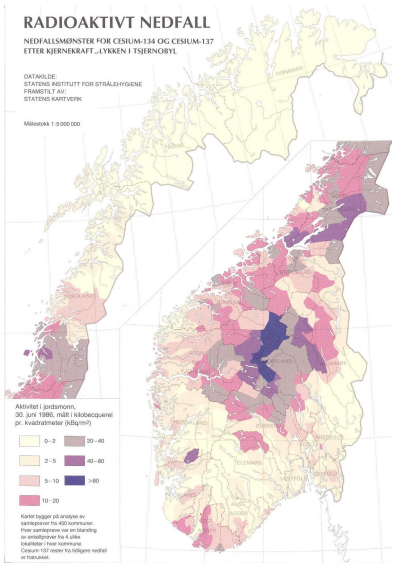

(a) Fallout over Norway after Chernobyl. Map supplied by DSA and the Norwegian Map Authority (Kartverket).

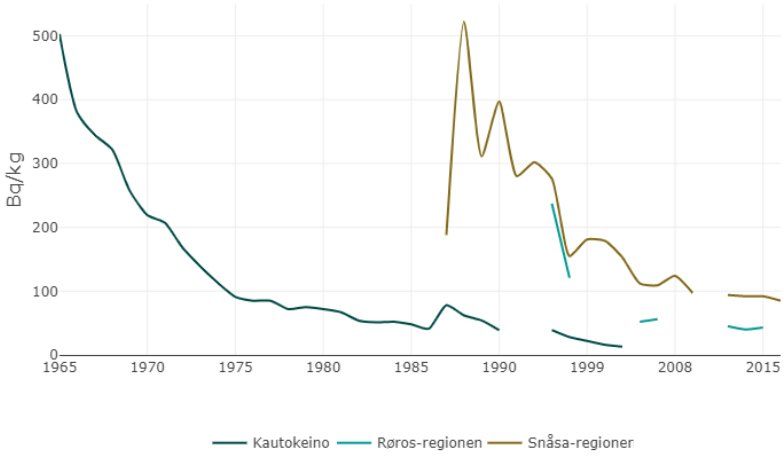

(b) Measurements of activity per unit mass of reindeer herders from 1965 to 2017. Three areas have been monitored, where Kautokeino saw a small increase succeeding the events in Chernobyl in 1986, while Røros and Snåsa saw larger changes, which is supported by the mapped fallout visualized to the left.

Figure 2.4

Chapter 3

Method

This chapter will display methods of how data is gathered both for measuring radioactivity in humans and for simulation. The focus is mainly to explicate the simulation of the calibration method, with a goal of improving the accuracy of real world measurements.

To measure the radioactivity, two different detectors are used, namely a NaI and a HPGe. These detectors are explained in sections 2.2.1 and 2.2.2. As with any other measuring devices the detectors periodically need to be calibrated. The calibration is done by using the IRINA phantom.

In the following sections, the method of calibration and the process of using Geant4 to simulate the calibration will be explained. All the phantoms and geometries contained in the mobile laboratory used by DSA are programmed into Geant4 in this thesis, so that simulations can be performed. This is called the simulation framework.

The terminology in the following chapters divide between results that are *measured* and *simulated*. Measured results are found through performed calibrations, and mainly data from 2012 is used. The simulated results are the results found in this thesis, using simulation in Geant4. Occasionally, also the calculated results will be mentioned, which are the theoretical data found through computation.

Parts of this chapter contain reworked parts from a smaller preparatory thesis, written by this very author. The goal of that thesis was to look into if there was potential of improving the real world measurements using the given method, which it concluded it was. The preparatory thesis used a significantly simplified model of what this report uses, which gave an idea of *some* of the problems that were needed to be tackled.

3.1 IRINA phantom

Several institutions in Europe are using the same geometry for calibrating detectors used for whole body measurements (Fonseca et al. (2014), Bochud et al. (2013)), which is called the IRINA phantom (Kovtun and Prokofyev, 1996). It consist of two types of blocks, big and small, that are used to build geometries in different sizes and positions. Today, DSA only use the geometries of sitting phantoms, but previously both the lying and bending (also known as the Palmer geometry (Lidén and Gustafsson, 1967)) geometries have been used. The blocks

are made of polypropylene. All six phantoms are virtually recreated in Geant4, as a part of the simulation framework.

The two different blocks have measurements width $W_b = 110\,\text{mm}$, length $L_b = 165\,\text{mm}$ and height $H_b = 55\,\text{mm}$, for the big block and width $W_s = 110\,\text{mm}$, length $L_s = 165\,\text{mm}$ and height $H_s = 25\,\text{mm}$ for the small blocks. Each block have two equally spaced out cylindrical holes going through the block lengthwise, with the holes placed $W_B/4 = W_s/4$ from the center of the width in each direction, as show in Figure 3.1. These holes are then filled with rods containing radioactive material, in this case ^{137}Cs. The rods have a radius of $r = 3\,\text{mm}$ and length $l = 163\,\text{mm}$.

Activity in the radioactive rods are given i table 1 in Kovtun and Prokofyev (1996) and repeated in Skuterud et al. (2013). Values are based on the activity measured at production 1 August 1996. There are two different types of rods, one for the big block and another for the small block. The activity at production are $A_{Big} = 242\,\text{Bq}$ and $A_{Small} = 121\,\text{Bq}$. With a half life of $T_{\text{Cs-137}} = 30.169\text{y}$, accurate activity of either a specific block or a whole phantom can be calculated for each day of measuring.

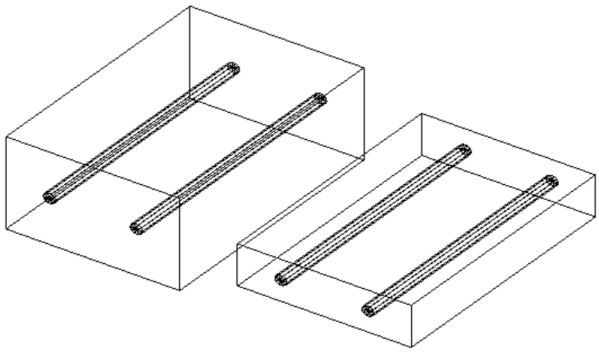

Figure 3.1: Building a phantom is done by stacking these two different sized blocks, here displayed with the radioactive source rods included.

The certificate by Kovtun and Prokofyev (1996) thoroughly describe how the different geometries are to be built; describing how many of the different block are to be used in each limb, and total numbers of block used. All geometries are assigned a name from P_1 to P_6, and are representing body sizes from a young child at mass $M_{P_1} = 10.6\,\text{kg}$ and height $H_{P_1} = 82.5\,\text{cm}$ to an adult with mass $M_{P_6} = 95.2\,\text{kg}$ and height $H_{P_6} = 170.5\,\text{cm}$. See Table 3.1 for the specifics. Figures 3.2 to 3.7 show how the phantoms were programmed into Geant4.

One of the weaknesses using the IRINA phantoms is that the largest geometry P_6 have a height of namely 170.5 cm, and since the average height for Norwegian men is, according to SSB (2014), 179.9 cm, the phantoms does not accurately represent an average man that DSA measures. And, Skuterud et al. (2013) confirms that height have significant importance for shielding radiation from the surroundings.

Table 3.1: Sizes of the IRINA phantoms

Phantom	Mass, [kg]	Height, [cm]	Height sitting, [cm]
P_1	10.6	82.5	44.0
P_2	20.9	121.0	66.0
P_3	40.9	160.0	77.0
P_4	61.5	170.5	88.0
P_5	77.8	170.5	88.0
P_6	95.2	170.5	88.0

Despite the name of the IRINA phantom, it has to be noted that they are made to represent the shape of men, not necessarily women. Given that the body shape widely varies between,

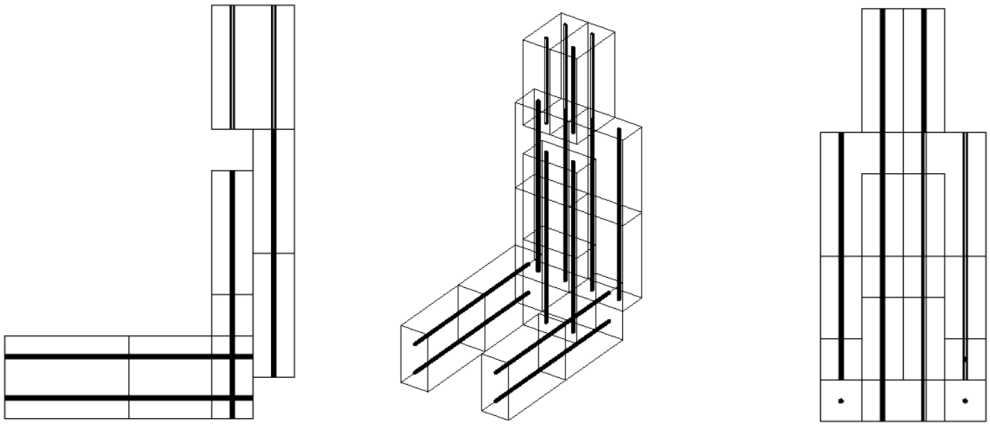

(a) Phantom P_1 from the side **(b)** Phantom P_1 **(c)** Phantom P_1 from the front

Figure 3.2: Phantom P_1 as programmed into Geant4. It is supposed to imitate a person with weight 10.6 kg and height 82.5 cm.

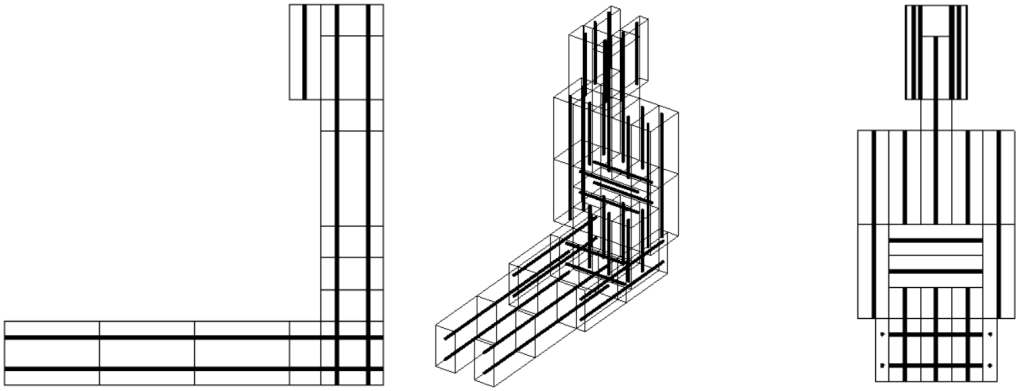

(a) Phantom P_2 from the side **(b)** Phantom P_2 **(c)** Phantom P_2 from the front

Figure 3.3: Phantom P_2 as programmed into Geant4. It is supposed to imitate a person with weight 20.6 kg and height 121.0 cm.

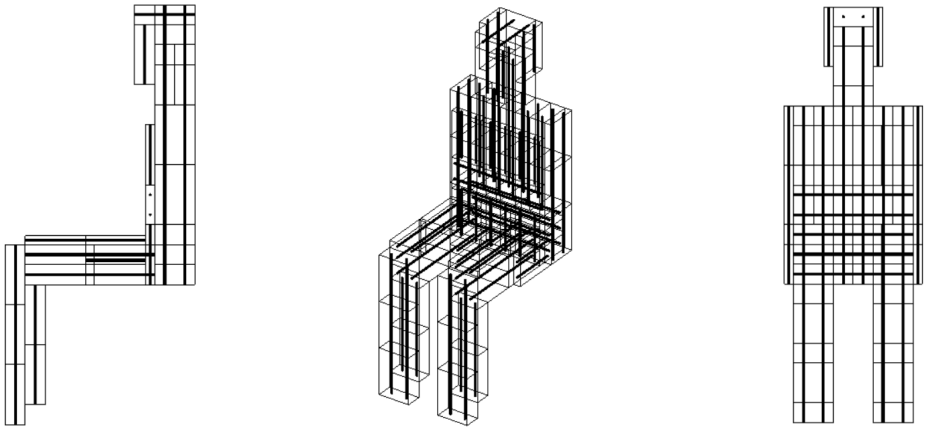

(a) Phantom P_3 from the side **(b)** Phantom P_3 **(c)** Phantom P_3 from the front

Figure 3.4: Phantom P_3 as programmed into Geant4. It is supposed to imitate a person with weight 40.9 kg and height 160.0 cm.

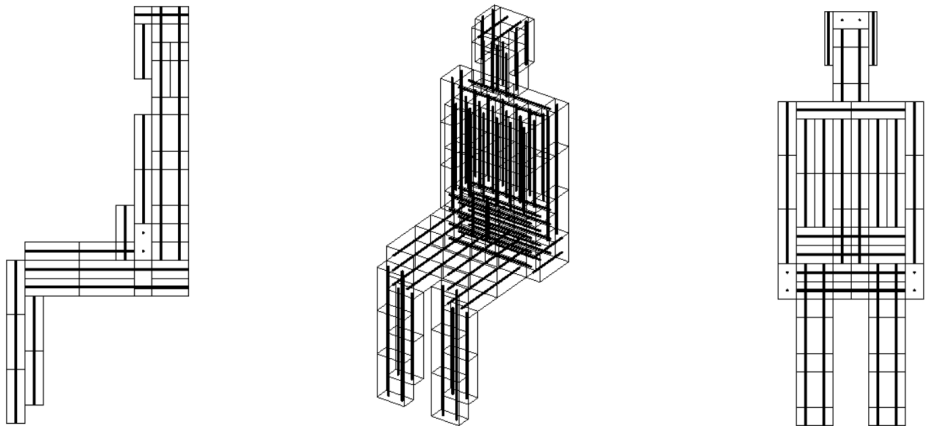

(a) Phantom P_4 from the side **(b)** Phantom P_4 **(c)** Phantom P_4 from the front

Figure 3.5: Phantom P_4 as programmed into Geant4. It is supposed to imitate a person with weight 61.5 kg and height 170.5 cm.

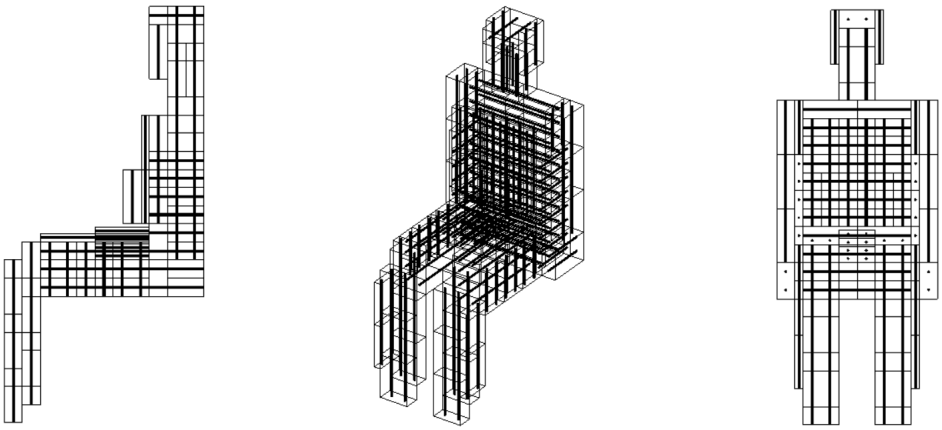

(a) Phantom P_5 from the side **(b)** Phantom P_5 **(c)** Phantom P_5 from the front

Figure 3.6: Phantom P_5 as programmed into Geant4. It is supposed to imitate a person with weight 77.8 kg and height 170.5 cm.

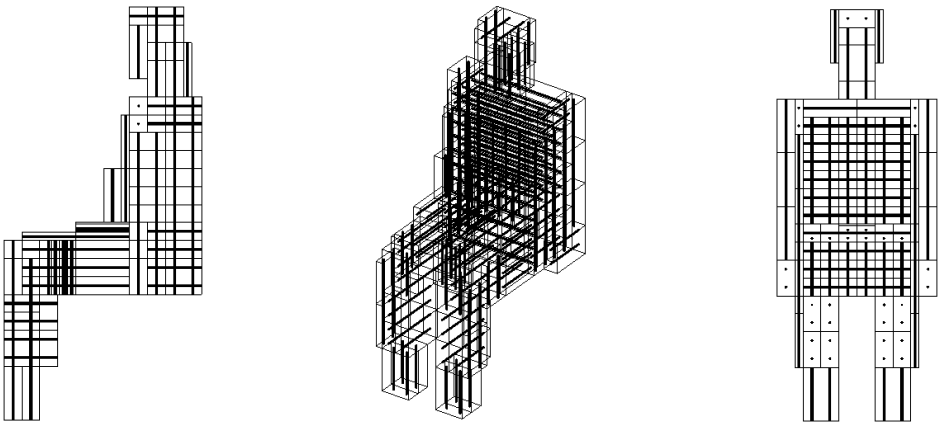

(a) Phantom P_6 from the side **(b)** Phantom P_6 **(c)** Phantom P_6 from the front

Figure 3.7: Phantom P_6 as programmed into Geant4. It is supposed to imitate a person with weight 95.2 kg and height 170.5 cm.

and among, the genders, the calibrations are still assumed to give a good enough representation. According to Hagerup-Jenssen (1996), who made simple measurements with phantoms with more woman-like shape, there where no measurable difference to those geometries to the measurements the IRINA phantoms provide. This is assumed to be due to the way cesium is treated in the body, close to identically as potassium, within the body (Leggett et al., 2003). Meaning that only negligible doses of Cs are found in fatty tissue, as the volume in the cell where Cs may travel through, are here occupied by fat. Radioactive material ingested into the gastrointestinal track (stomach, small and large intestine) is then transported either out through fecal excretion or into the blood stream (from the small intestine). From the blood, ICRP (1989) uses a two chamber model for further transportation: the radioactive material either continue to flow through the blood stream with short biological half life, or distributed into soft tissue where the material move as free ions with a longer biological half life. The material the is transported out of the body through urinal excretion.

Set standard by ICRP (1989), ^{137}Cs is found to have a biological half life of $T_1 = 2$ days and $T_2 = 110$ days in their particular chambers. About $\rho_1 = 10\,\%$ of radioactive material going through the blood continues to do this, while $\rho_2 = 90\,\%$ is distributed into soft tissue. Added to this, the isotopes are found to have an additional $T_b = 6$ hours biological half life in the blood before potentially distributed into soft tissue. These biological features are approximated to be insignificant in difference between genders, resulting that the IRINA model is assumed gives reliable measurements also for women.

Using MC simulations of the calibration method, DSA wants to examine which features could be taken into account and result in improved output data. As of fall 2019, over 33 years since the Chernobyl accident, the amount of ^{137}Cs in the fallout area is naturally halved, thus measured values are correspondingly lower. Following this, it is harder to distinguish measured objects from the background noise. DSA therefore wish to address this problem by looking at variables to enhance accuracy on low-level whole body measurements, as this equipment is valuable for measuring people in general, not only reindeer herders. Accurate measurements would be beneficial in the future for both academic reasons and for public health.

3.2 Measuring radioactivity in humans

DSA is in possession of a container which contain detectors and setup. The container is divided into two rooms, one of which contains the setup, see Figure 3.8 how it is implemented into Geant4. Inside, a 25 cm high plateau is placed to the side of the room, which upon an adjustable chair, detector stand and a protection wall behind the chair is installed. Both the plateau and the back wall contains a 5 cm thick Pb core. Exact measurements and placements of these objects have been important when creating a replica in the simulation program and will be given in section 3.3.

The object that is to be measured is placed into the chair, adjusted 68.5 cm above the podium. The detector is then placed in at a set distance in front of the object at an 30° angle downwards. Collimation of the detector is 2 cm and the detector position is set to 15.5 cm on the detector-rack. This corresponds to that the detector is placed approximately 114 cm above the podium and 40 cm from the back of the chair, easily seen in Figure 3.8a.

The two detectors DSA operates, described in section 2.2, is a HPGe- and a NaI-detector. The HPGe is a Ortec model named GEM50P and is a ”Pop Top” type, with serial number

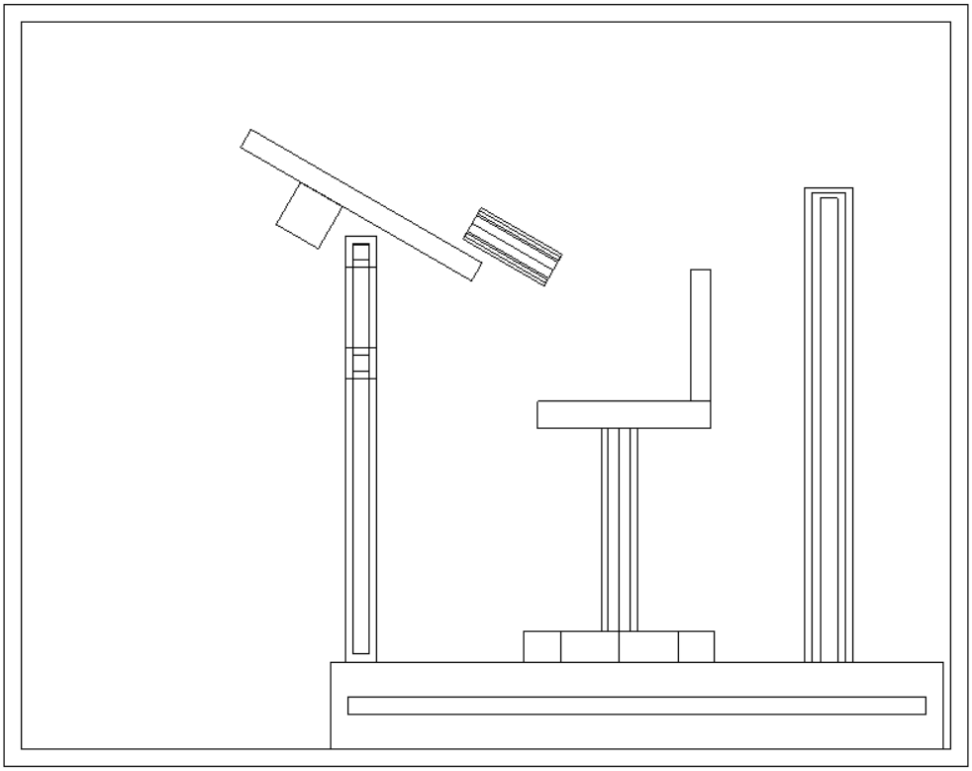

(a) Container from the side

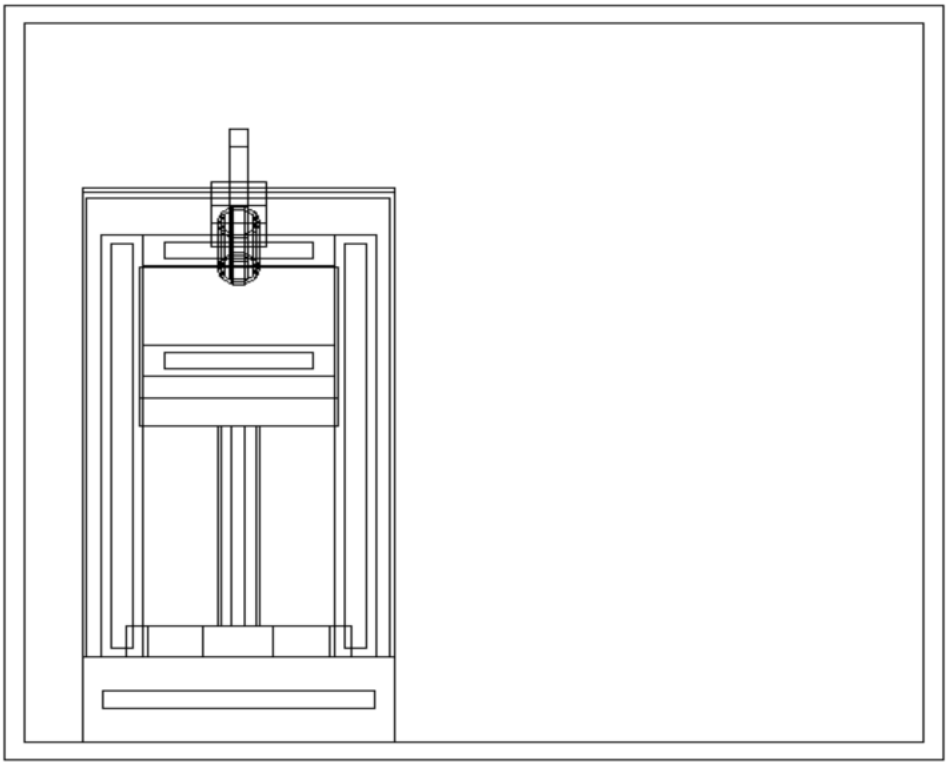

(b) Container from the front

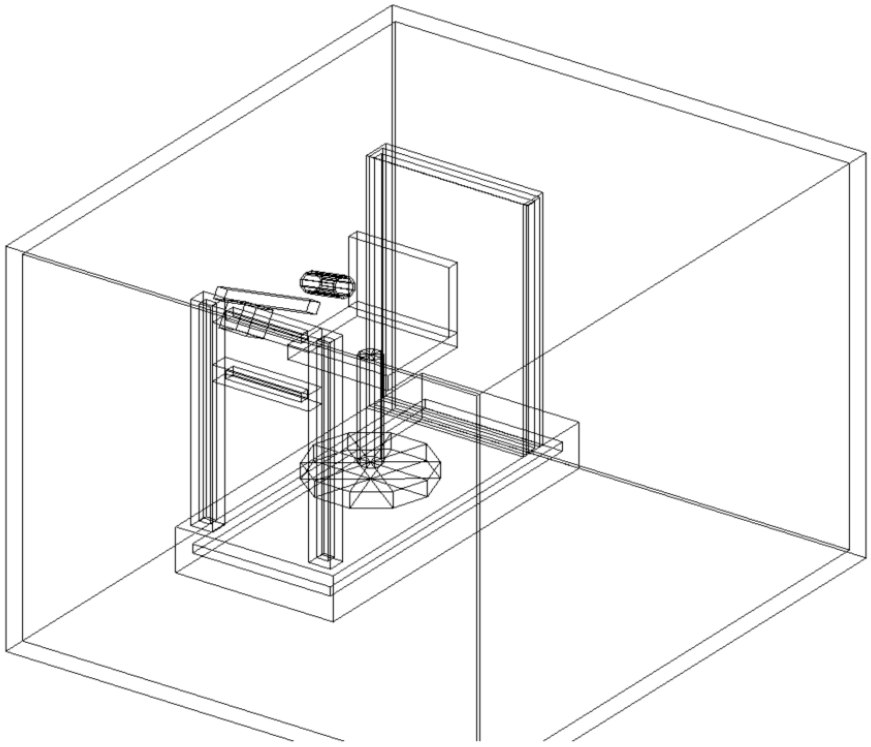

(c) Container from an angle

Figure 3.8: The container as constructed within Geant4, containing 5 cm thick walls, plateau, chair, detector stand and a back wall for protection.

43-TP21634A and resolution 1.9 keV at 1.33 MeV. Peak-to-Compton radio is 66:1. The NaI detector have serial number 2665 and the model is a 76s76 Crismatec (Scintibloc).

Measurements are then set to last for 20 min for each person. Measured time, in seconds, is important, so that the amount of counts registered by the detector combined can be calculated into activity, A. Before measurements of people it is necessary to perform a baseline measurement (measurement without anything in the chair) over a longer period of time (at minimum 30 min, but as long as possible), such that background radiation can be subtracted from a measured person. It have also been tested to measure a phantom of sugar (doesn't radiate) to give a approximate idea of the amount shielding form surrounding radiation a person do when measured (Skuterud and Thørring, 2012).

3.3 Calibration setup in Geant4

Using Geant4 through Visual Studio 2017 the setup has been constructed using the same principle as when DSA perform calibration of the detectors. Blocks of polypropylene is built like LEGO to mimic the different IRINA geometries. The holes in the blocks are filled with rods of ^{127}Cs. The following section will describe measurements and simplifications that were made to build the simulation framework.

When creating the phantoms within C++, it was assumed a perfect build, hence the angle of both knees and hip were assumed to be 90°. Figure 3.9 shows the IRINA phantom when assembled into two different phantom sizes.

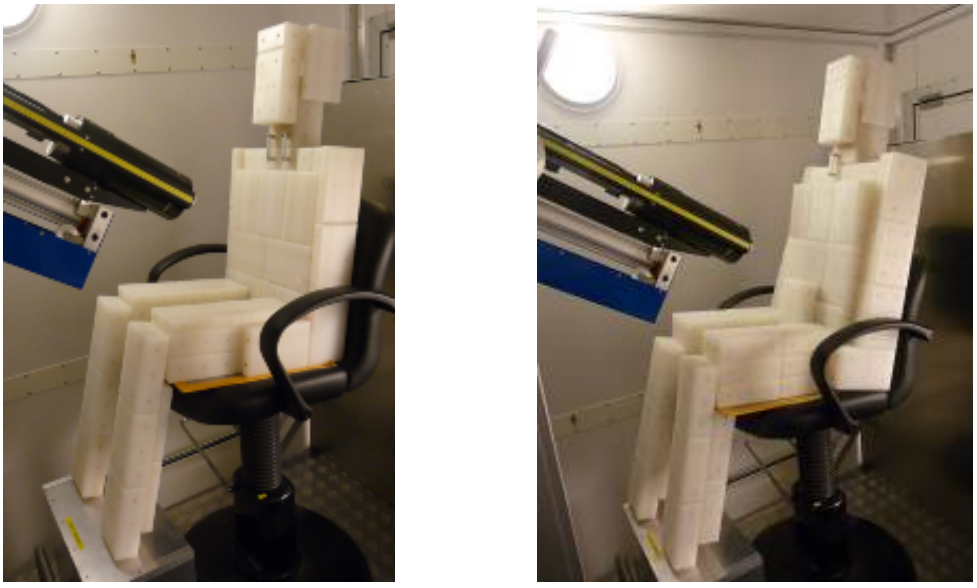

Figure 3.9: Phantom P_3 and P_4 when placed into the chair in the laboratory. In difference to the simulated setup, the angle at knees and hips are clearly not 90° as a perfect build would be.

3.3.1 Construct a geometry in Geant4

Geant4 requires a specific way to create an object for the simulations to work. First a `world` volume must be created, defining the largest volume the simulations exist within. Every feature or object must be fully enclosed in the defined `world`. Next, each object (including

world) has three layers of creation, making Geant4 a powerful and efficient way to construct repeating patterns. First layer is to define a solid object, using e.g. the functions G4Box and G4EllipticalTube, where the name of the object and its dimensions are chosen. Then a logical volume is created, taking an existing solid object and assign a (predefined) material to it and giving it a new name. This process makes is easy to take a solid of a specific geometry and recreate it in different materials. Next, the actual feature is made, by creating a physical volume. A physical volume is made using the G4PVPlacement($\cdot$) function, which requires the arguments: rotation, placement, logical volume to be placed, name, logical mother volume, boolean expression and copy number. What this allows for, is to place a logical volume into another logical volume, making a more complex geometry which can be repeatedly placed in multiple positions and rotations.

For this particular setup, the two different sized blocks and the ^{137}Cs rods were constructed as three different logical volumes, using their respective specification. Then it was possible to use G4PVPlacement($\cdot$) twice, to place rods into the logical volume for each of the two different blocks, making the rods a property of the blocks. Furthermore, the blocks could be placed repeatedly into the world.

To create a phantom, each block was separately positioned into a rectangular world, called envelope (not visible in Figures 3.2 to 3.7), specifying each placement, rotation and copy number. Each envelope has dimensions equal to its corresponding phantom, making it easier to place blocks accurately.

Using the same method, the rest of the container could be constructed and carefully placed. This was done in a separate script, keeping each phantom and the container in separate scripts. By writing the phantoms to .txt-files, it was possible to read the phantoms into the container as a single logical volume, making placement within the container easy. Though the phantoms could be operated as one single logical volume, this method also made it possible for the container script to access both blocks and Cs rods within the phantom.

Within the script where the the container was created, each feature (chair, plateau etc) was written as functions, making it simple to remove a feature if necessarily.

3.3.2 Specifications of the mobile laboratory

The container was measured to have inner dimensions of width 2.31 m, height 2.10 m and length 2.68 m. As the setup is placed sorely in one half of the container, with the detector directed away from the other half, only this part is implemented; which gives the constructed container half the length of what the real container is. In Figure 3.10 the orientation of vectors as defined by Geant4 is shown. All wall was found to be 5 cm thick and chosen to be filled with aluminium.

Looking at Figure 3.8a it is clear that the setup is placed upon a podium, 25 cm high, measuring 80 cm in width and 177 cm in length, located to the left of the room 15 cm from the side wall and 2 cm from the back. A Pb core, 5 cm thick, going almost the full length of the plateau is placed in the middle, surrounded by aluminium. The chair is placed approximately in the center, only offset by 5 cm lengthwise towards the front. Following the instructions of DSA calibration specifics, the chair height is set to 68.5 cm above the plateau. Chair material is set to some aluminium (base and leg) and some non-interacting plastic material, here chosen to polypropylene for convenience.

Behind the chair, the protection wall is set up to prevent radiation from the surroundings to

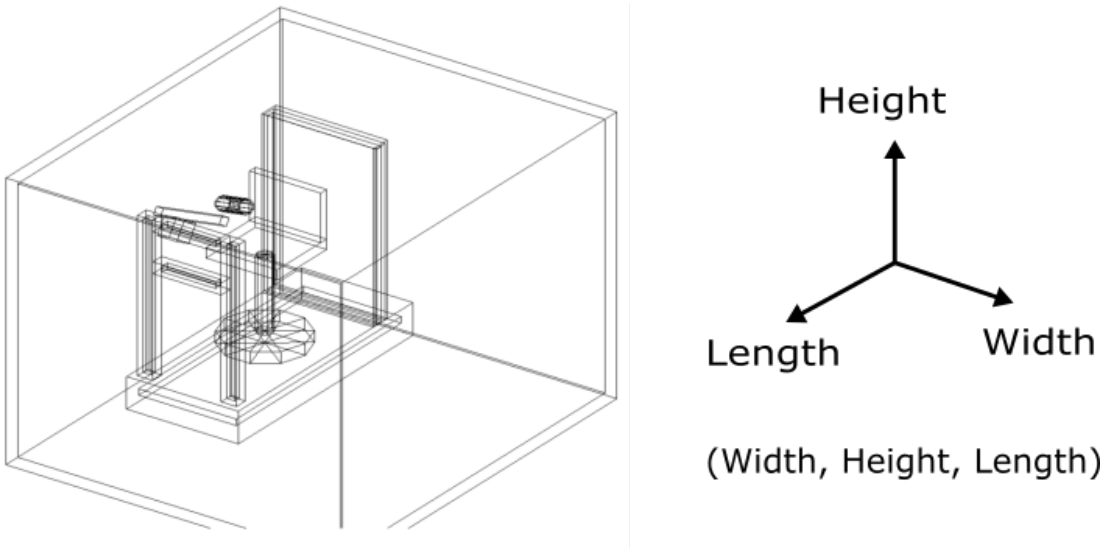

Figure 3.10: Illustration of how Geant4 chooses vector orientation and how they are labeled. The origin is set to be in the middle of the container. Geant4 operates using half-lengths, meaning that an input yields double the size. Making a box of dimensions 1 m × 2 m × 4 m, Geant4 require the inputs $x = 0.5$ m, $y = 1$ m and $z = 2$ m.

interfere with the measurements and to prevent measuring backscattering from the person. The wall is 137 cm high from the podium, fills the podium in the width and is 14 cm thick. It contains, as the podium, a 5 cm slab of lead in the center, and is made of a scaffolding of aluminium, thus constructed as a block of 50 % aluminium and 50 % of air. This wall is placed 28 cm in front of the container wall.

Next, the detector stand is placed 47.5 cm in front of the chairbase, reach 123 cm upwards and consist of two rectangular legs, each placed 35.5 cm from the center of the plateau. The upper section of the stand is angled 30° downwards, set as standard by DSA, and consist of a bar, a holder for the detector and a cube of lead as counterweight, see Figure 3.8a. To collimate the detector, DSA has set a 2 cm gap from the detector surface to the end of the tube which holds the detector. This tube is also made of lead.

It was chosen to make independent scripts in Geant4 for creating the phantoms and read those into the main code running the simulations. This was done in an attempt to increase the readability of the code, make it easier to adjust and to decrease the size of the code.

3.3.3 Scoring hits at detector surface

Next step of simulating is to declare the amount of radiation released from the rods. This was done using the G4GeneralParticleSource class, creating an envelope volume enclosing the whole phantom and assign all geometries within this volume with characteristics of the ^{137}Cs-rods to each emit gamma particles isotropically at an energy of 662 keV. Then, set the total amount of particles emitted within the confined volume using the command `run/beamOn`. In appendix A, some macros is provided to show how this works.

Implementation of the detector is done by a scoring volume; a user defined volume that registers the particles flowing through it and their corresponding energy. It was chosen to make a circular volume 1 cm thick and with radius 4.5 cm, close to the specific detectors DSA hold. Naturally, the scoring volume was placed into the detector holder tube, 2 cm from the end. To be able to do some extra analyzing, the scoring volume was divided into smaller

so-called `bins`; section of the circle. Specifically, 20 azimuthal sections and 30 in the radial direction, thus 600 sections in total, see Figure 3.11 for an illustration. Dividing the thickness of the scoring volume in more than one section could give information on the direction of the photons, however this is not in the purpose of this thesis.

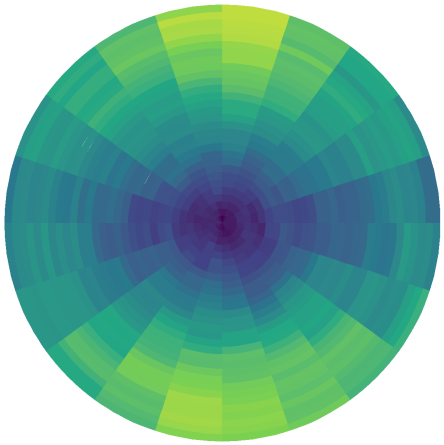

Figure 3.11: Illustration of the scoring volume made in Geant4. The circle is divided into 20 angular sections, 30 radial rings and one slice into the paper, making it containing a total of 600 small volumes, called `bins`. This particular detector surface is made by using the result when simulating 10 million emissions from phantom P_1 the first of five times.

Results where then written to file in respect to energy. Yet again defined by DSA, the region of interest (ROI) was found to correspond to the energy interval 657 keV to 665 keV (Skuterud et al., 2013). Three files where saved, one containing the counts within the given interval, called *Peak*, one containing counts for all energies below and one containing the ones for higher energies. The detectors and software DSA hold registers the count of photons into channels, rather then energy. But, knowing the value of the Bragg peak for ^{137}Cs at 662 keV (Helmer and Chechez, 2017), these channels can be calculated into their corresponding energy.

3.3.4 Performing simulations to test the framework

The first simulation was a set of baseline measurements. Each phantom was set to emit a total of 10 million photons (or events), to register how the detector register the difference in size between the phantoms. Using the data given in the saved files, calculating the efficiency of the two detectors for the different phantoms were possible. This done in total five times, giving a broader set of data to increase the cogency of the simulations and results. The reason for choosing 10 million events distributed over five runs, is due to the time used for each simulation. An external computer was set up, such that simulations could run separately on this powerful computer, rather than using a normal laptop, which have constraints on computational power. This made the simulations able to run near continuously for several weeks, supplying results.

Continuing, calibration results from 2012 and 2015 was reproduced within Geant4 to give information on the difference of the constructed and the real setup. Activity for the phantoms at calibration date, using (2.6), multiplied by live time (time used for calibrating) and the emission probability of ^{137}Cs, $\phi = 0.85$, gives the total number of events during the measuring period. The expectation for this was to be able to get expression on the form

$$N_s = C_{P_i} \cdot N_c, \qquad i = 1,2,...,6 \tag{3.1}$$

where N_s is the number of counts registered in the simulation, C_{P_i} a constant for each phantom and N_c the counts measured during calibration.

Due to the assumption of a perfect build for both phantom and features within the container,

some deviations from the calibration results were expected. A particular inconsistency was the back of the chair, which in the physical container is curved, giving room for the wider phantoms to sit slightly nearer the detector than the small phantoms. To look at this, some simulations adjusting P_1 nearer and further away from the detector was executed. Specifically, four runs (with 10 million events each) adjusted 5 and 10 cm forwards and 5 and 10 cm backwards.

Lastly, a set of simulations to look at the shielding of surrounding radiation performed by each phantom was executed. As the container is made portable, measurements regularly is executed in radioactive contaminated areas, such as Snåsa. Thus, a slab of air underneath and around the container was set to emit a uniform amount of radiation, also with ^{137}Cs-characteristics. The slab of air was chosen to be 5 cm thick and filling the whole area defined as the world in Geant4, resembling the ground the container stand upon. Here, a set of simulations with 100 million events where performed with each of the phantoms sitting in the seat.

Illustrated in Figure 3.12, a run of 100 events of gamma emission from the sources. This figure is provided as a visual aid to see what the simulations do. In Figure 3.13 the same is done, only using the actual activity of P_4 at 20th November 2019.

Comparing different geometries of the IRINA phantom, grants information of the amount of surrounding radiation shielded by a geometry as a function of phantom shape and size. It also allows to compare measured values when the HPGe detector last was calibrated against the simulated values. This will potentially give information of the accuracy of the measurements done after this calibration.

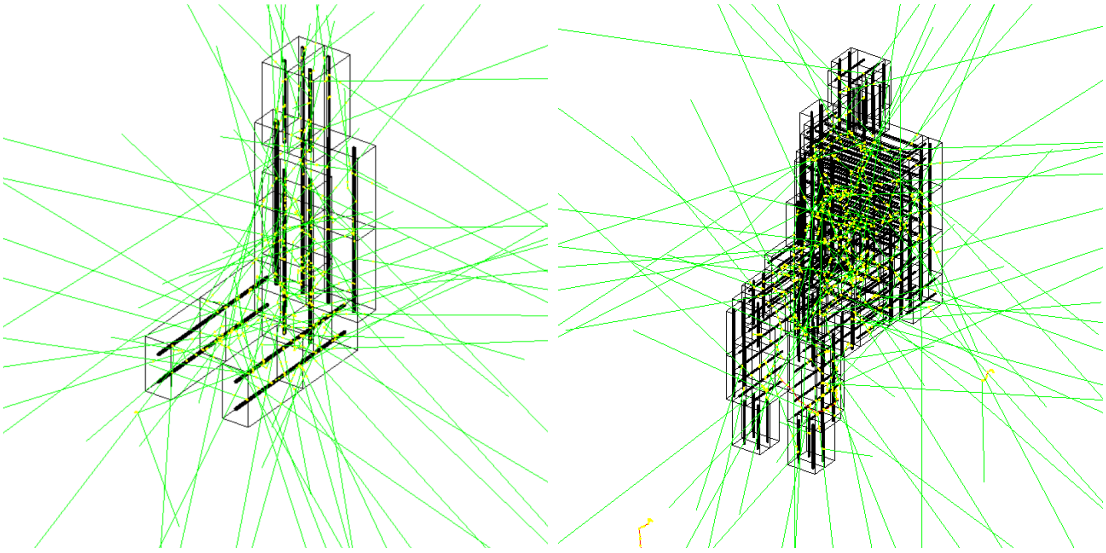

(a) Phantom P_1 **(b)** Phantom P_6

Figure 3.12: An instance of 100 events of gamma emission from the ^{137}Cs sources, as a visual aid for what the simulation do. The green lines are photon track, the red are electrons released as photoelectrons and the yellow dots are points of interaction

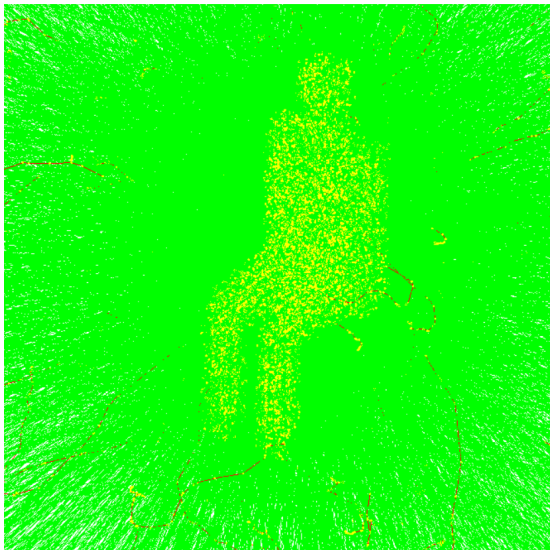

Figure 3.13: An illustration of one second of activity in phantom P_4. The number of simulated events is equal to the number of photons released each second, $A = 19835\,\text{Bq}$, at 20th November 2019 . Green lines are photon tracks, red lines are photoelectrons and yellow is points of interaction and are the only way to see the outline of the phantom.

Chapter 4

Results

The main result of this thesis is the written code using Geant4 and C++. The code is submitted to DSA and allows them to perform further simulations and measurements to improve the accuracy when measuring radioactivity in humans. Some of the macros used to control the simulations are shown in appendix A.

To test and verify the robustness of the code, several simulations, as explained in section 3.3.4, were performed. The rest of this chapter will look at the results of said simulations.

Visualization of all phantoms as implemented into Geant4, each placed into the chair in the container, can be examined in Figure 4.1.

4.1 Baseline simulations; 10 million events

By running 10 million events for each of the phantoms, it is possible to make repeatable simulations that can easily be reproduced. In this thesis it was used to repeat the same simulations multiple times, as the chosen amount does not require a "better than normal" computer to complete the simulations in a reasonable time. This particular simulation was repeated five times, resulting in a total 50 million events for each phantom. The counts and efficiencies from the simulation can be viewed in Table 4.1. Measured efficiencies from calibration, $\varepsilon^m_{\text{HPGe}}$ and $\varepsilon^m_{\text{NaI}}$, are provided from Skuterud et al. (2013), while the simulated efficiency, ε^s, is found by dividing *Peak* by the total number of simulated emissions for each run, 10 million. For comparing measured and simulated efficiencies, the values were normalized by introducing

$$\kappa_{\text{dec}} = \frac{\varepsilon^s}{\varepsilon^m_{\text{dec}}}, \qquad \text{dec} = \text{HPGe or NaI.} \tag{4.1}$$

In Figure 4.2a and 4.2b the normalized values are displayed, while Figure 4.3 shows the simulated efficiency for each phantom. DSA have not performed calibrations using P_6, neither calibrating the NaI-detector using P_1.

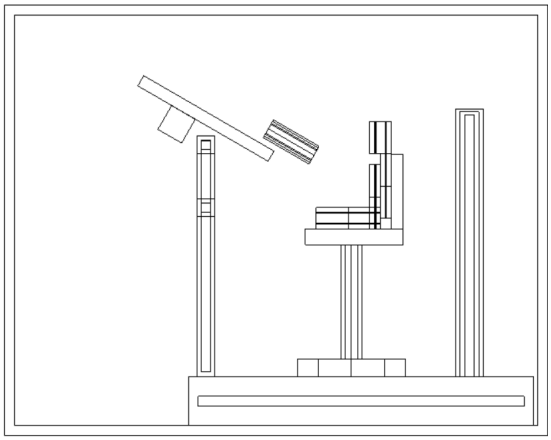

(a) Phantom P_1 sitting in container.

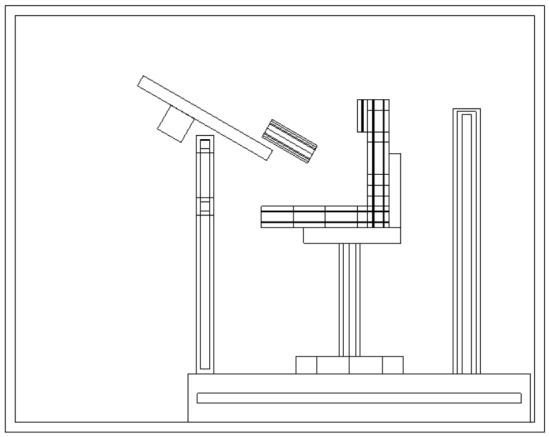

(b) Phantom P_2 sitting in container.

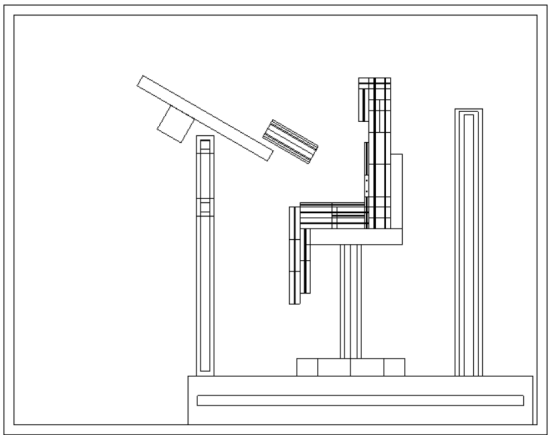

(c) Phantom P_3 sitting in container.

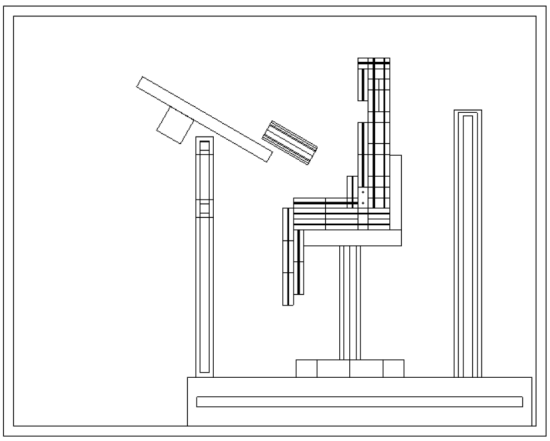

(d) Phantom P_4 sittingin container.

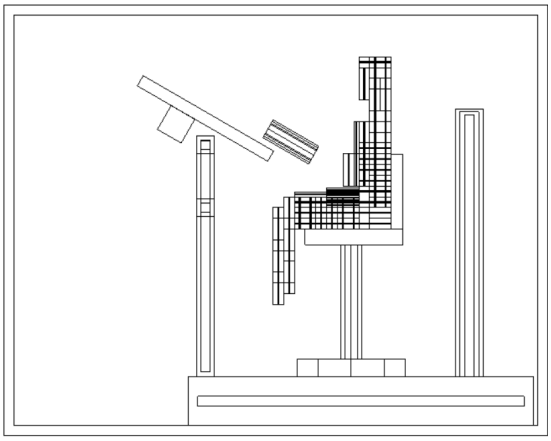

(e) Phantom P_5 sitting in container.

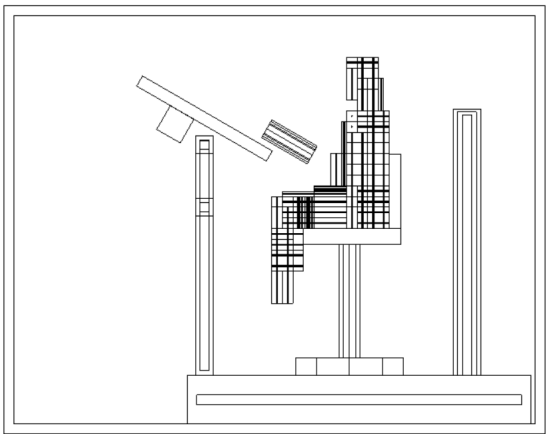

(f) Phantom P_6 sitting in container.

Figure 4.1: Side view of all phantoms sitting in the chair within the container, containing all notable features, such as the plateau, protection wall and detector stand. This is the how Geant4 see the phantoms when running the simulations. The scoring volume was placed in the cylinder in front of the phantoms by accurately calculating the position, 2 cm collimated.

Table 4.1: Simulated results, *Peak*, when simulating 10 million events for each phantom, five times. The simulated efficiency ε^s is compared to the efficiencies found during calibration, $\varepsilon^m_{\text{dec}}$ for both detectors, NaI and HPGe. The number of counts, *Peak*, is the amount of counted photons within the inspected energy spectrum. The two last values, κ_{dec}, are the relative relationship between calibrated and simulated efficiencies. For P_6, no reliable calibration results have been registered. For P_1 no calibration with the NaI detector has been performed. Values $\varepsilon^m_{\text{dec}}$ are the average efficiency found during calibration in 2012, excluding $\varepsilon^{m,P_1}_{\text{HPGe}}$ which is provided from calibration in 2015.

Phantom	Run	Peak	ε^s	$\varepsilon^m_{\text{HPGe}}$	$\varepsilon^m_{\text{NaI}}$	κ_{HPGe}	κ_{NaI}
P_1	1	105438	0.0105	0.000240		43.9	
	2	102090	0.0102			42.5	
	3	100338	0.0100			41.8	
	4	102227	0.0102			42.6	
	5	100889	0.0101			42.0	
P_2	1	104778	0.0105	0.000223	0.000489	47.0	21.4
	2	102806	0.0103			46.1	21.0
	3	104535	0.0105			46.9	21.4
	4	103212	0.0103			46.3	21.1
	5	100201	0.0100			44.9	20.5
P_3	1	98345	0.0098	0.000193	0.000425	51.0	23.1
	2	97643	0.0098			50.6	23.0
	3	98175	0.0098			50.9	23.1
	4	98257	0.0098			50.9	23.1
	5	98137	0.0098			50.8	23.1
P_4	1	84595	0.0085	0.000167	0.000367	50.7	23.2
	2	85451	0.0085			51.3	23.3
	3	86208	0.0086			51.6	23.5
	4	86518	0.0087			51.8	23.6
	5	85552	0.0086			51.2	23.3
P_5	1	96333	0.0096	0.000169	0.000373	57.0	25.8
	2	97878	0.0098			57.9	26.2
	3	96574	0.0097			57.1	25.9
	4	97438	0.0097			57.7	26.1
	5	95626	0.0096			56.6	25.6
P_6	1	104672	0.0105				
	2	102545	0.0103				
	3	105763	0.0106				
	4	104072	0.0104				
	5	102759	0.0103				

4.2 Recreating calibration results

For recreating the calibration results from 2012, the report from Skuterud et al. (2013) supplied the raw data used for carry out simulations. Table 4.2 and 4.3 display live time (measurement duration), measured entries in ROI into detectors during calibration, calculated activity for each phantom $d = 5814$ days after production, entries into simulated scoring volume for photons in the set ROI (Peak), measured efficiency of detector $\varepsilon^m_{\text{dec}}$ and simulated efficiency $\varepsilon^s_{\text{dec}}$. As the simulations are done without noise and are independent of detector efficiency, these efficiencies are significantly higher than the ones found during calibration.

Efficiency of the detector, $\varepsilon^m_{\text{dec}}$, is provided by DSA and contains information about both the efficiency of this particular detector and efficiency of the different phantoms, while $\varepsilon^s_{\text{dec}}$ only accounts for the geometrical efficiency by the phantoms. As the detector geometry was not

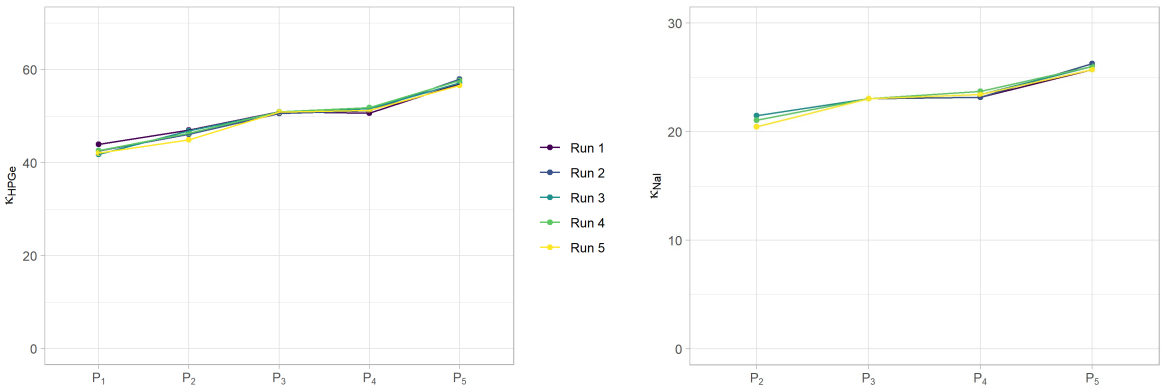

(a) Calibrated results from 2012 using HPGe detector, compared to simulated results.

(b) Calibrated results from 2012 using NaI detector, compared to simulated results.

Figure 4.2: Calibrated efficiencies of each phantom normalized by dividing on their corresponding simulated efficiencies, as a function of phantoms. All five runs are plotted, showing correlations between each run for each phantom.

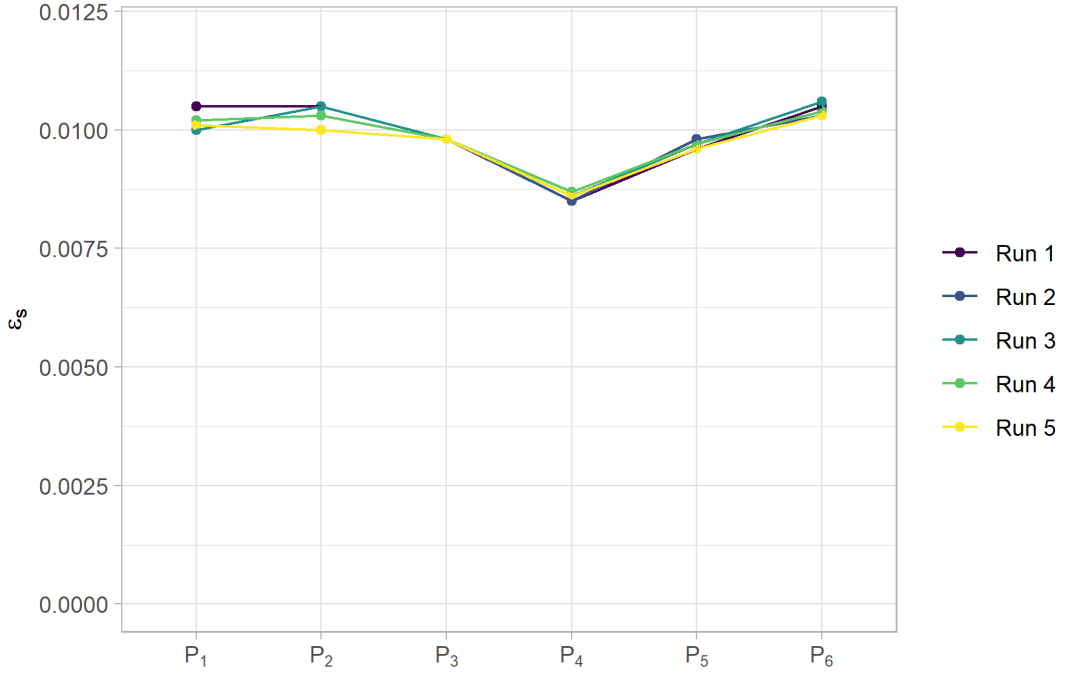

Figure 4.3: Simulated efficiency in each phantoms.

simulated, dividing $\varepsilon^m_{\text{dec}}$ by $\varepsilon^s_{\text{dec}}$ for each run should ideally give a constant value, describing the detector dependence.

4.3 Moving a phantom in the chair

Figure 4.4 display the slight changes that where made to look into the effect of proximity to the detector. The smallest (and least wide) phantom P_1 was shifted into four positions placed $\Delta l = \pm 5\,\text{cm}$ and $\Delta l = \pm 10\,\text{cm}$ lengthwise, while staying at the same height and width. Each position was simulated with 10 million events. These results where compared to the

Table 4.2: Calibration data from 2012, using a HPGe detector. Measured counts, *Integral*, compared to simulated counts, *Peak*, are the numbers of photons hitting said detector or scoring volume, within the live time at a given energy interval. Their corresponding efficiencies are given by $\varepsilon^m_{\text{HPGe}}$ and $\varepsilon^s_{\text{HPGe}}$. The activity is the amount of photons emitted pr second, in all directions.

Phantom	Run	Live time, [s]	Integral	Activity, [Bq]	Peak	$\varepsilon^m_{\text{HPGe}}$	$\varepsilon^s_{\text{HPGe}}$
P_2	1	6428.1	13106	8057.9	452352	0.000229	0.0103
	2	6255.9	12440		447579	0.000217	0.0103
P_3	1	5826.9	18702	16787.3	807790	0.000193	0.0097
	2	6800.9	21795		956137	0.000192	0.0099
P_4	1	4595.6	17477	23502.3	790087	0.000167	0.0086
	2	4071.4	15413		699033	0.000166	0.0086
P_5	1	3330.2	15951	30217.2	1017139	0.000168	0.0119
	2	1182.5	5702		364633	0.000170	0.0120

Table 4.3: Calibration data from 2012, using a NaI detector. Measured counts, *Integral*, compared to simulated counts, *Peak*, are the numbers of photons hitting said detector or scoring volume, within the live time at a given energy interval. Their corresponding efficiencies are given by $\varepsilon^m_{\text{HPGe}}$ and $\varepsilon^s_{\text{HPGe}}$. The activity is the amount of photons emitted pr second, in all directions.

Phantom	Run	Live time, [s]	Integral	Activity, [Bq]	Peak	$\varepsilon^m_{\text{NaI}}$	$\varepsilon^s_{\text{NaI}}$
P_2	1	6566.2	64253	8057.9	465220	0.000489	0.0103
	2	4882.3	47736		345030	0.000488	0.0103
P_3	1	62972.6	774830	16787.3		0.000423	
	2	4254.0	52567		599247	0.000427	0.0099
P_4	1	3152.1	42940	23502.3	537861	0.000368	0.0085
	2	2600.0	35269		443182	0.000365	0.0085
P_5	1	1242.5	19676	30217.2	375026	0.000372	0.0118
	2	1281.4	20349		319821	0.000374	0.0097

results of P_1 given in Table 4.1. In Figure 4.5 the numerical efficiency in all positions are displayed, with the simulated differences being significantly lower in the position furthest away compared to the position nearest the scoring volume.

The number of counts for each displacement is shown together with their corresponding efficiency and the fraction of counts compared to the average *Peak* of the three measurements of P_1 given in Table 4.1.

4.4 Shielding by phantoms from surrounding radiation

To test the shielding of surrounding radiation done by each phantom, i.e. how much of the radiation from the surroundings is blocked by the phantom, six simulations were performed; one for each phantom. A slab of air was put underneath the container and its surroundings, representing the ground. Runs with 100 million events where simulated, where all radiation where emitted from the slab, none from the phantoms. Table 4.4 shows both the registered photons within the ROI and the total amount of photons that hits the scoring volume. Also, the fraction of total registered photons relative to P_1 is shown. Figure 4.6 serve as a visual aid for the process, displaying 3000 emitted photons with P_3 placed in the chair.

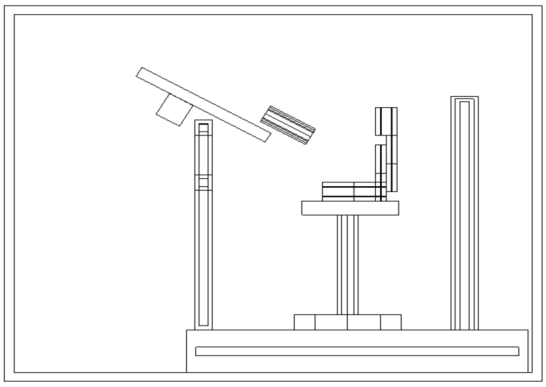

(a) Phantom P_1 sitting 5 cm further away from the detector.

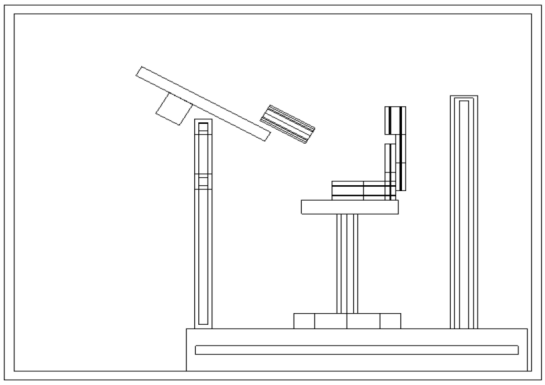

(b) Phantom P_1 sitting 10 cm further away from the detector

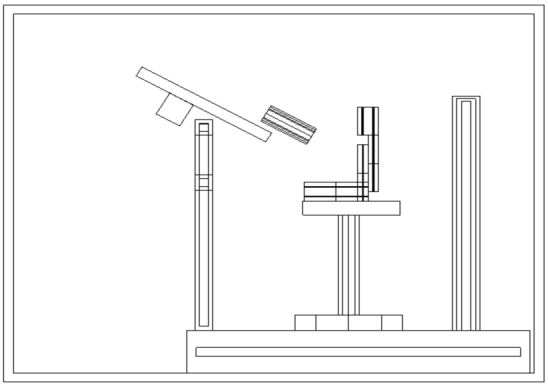

(c) Phantom P_1 sitting 5 cm nearer the detector.

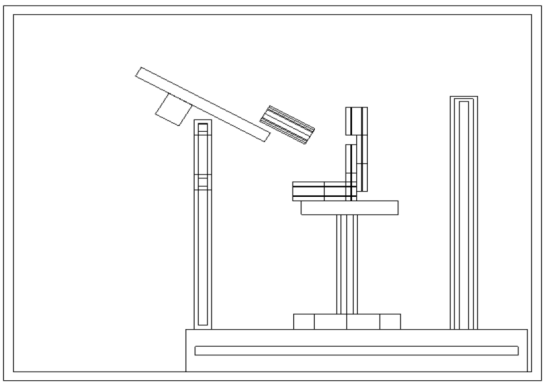

(d) Phantom P_1 sitting 10 cm nearer the detector

Figure 4.4: Shifting P_1 nearer and further away form the detector. The back of the chair is removed to easier complete the measurements and to get a more consistent result for every phantom positioning. Positioning is done by altering the y coordinate in Geant4.

Table 4.4: Registered number of photons into the scoring volume in a radioactive contaminated area. Each phantom is simulated with 100 million events emitted from the ground. In *Fraction, total*, the relative fraction of the numbers in *Total* compared to that of P_1 is presented.

Phantom	Peak	Total	Fraction, total
P_1	622	4253	1.000
P_2	873	4086	0.960
P_3	564	4119	0.969
P_4	741	3626	0.853
P_5	577	3057	0.718
P_6	461	3042	0.715

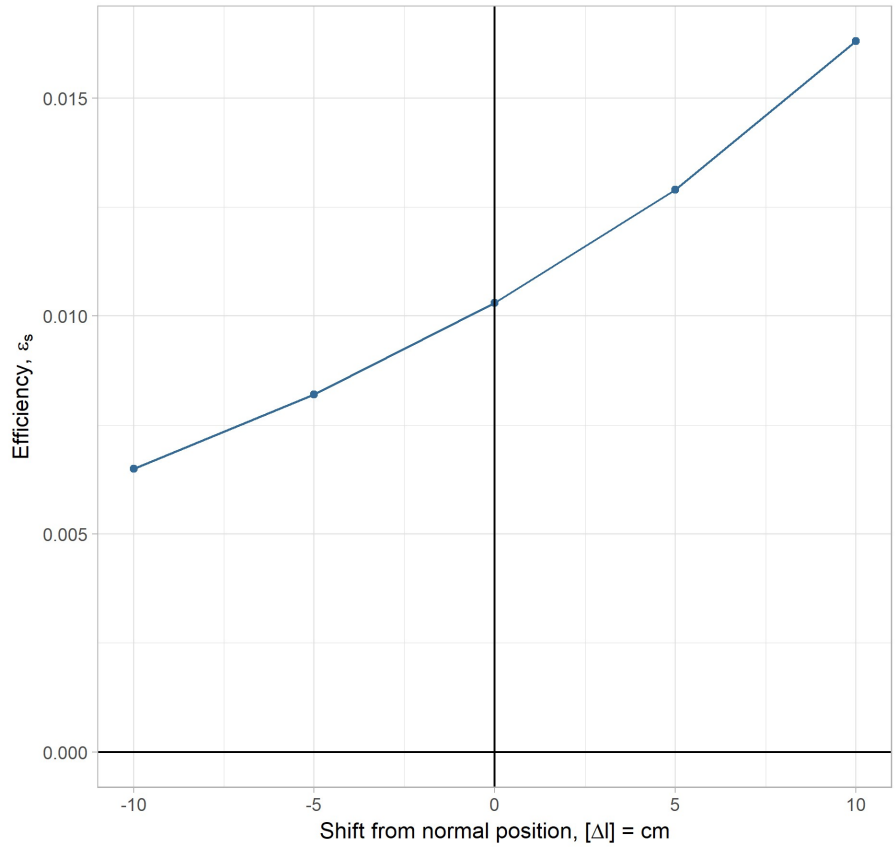

Figure 4.5: Efficiency result from the scoring volume when simulating 10 million events of P_1 when places in positions nearer and further away from the scoring volume. Zero is defined at the normal placement, with the back into the chair.

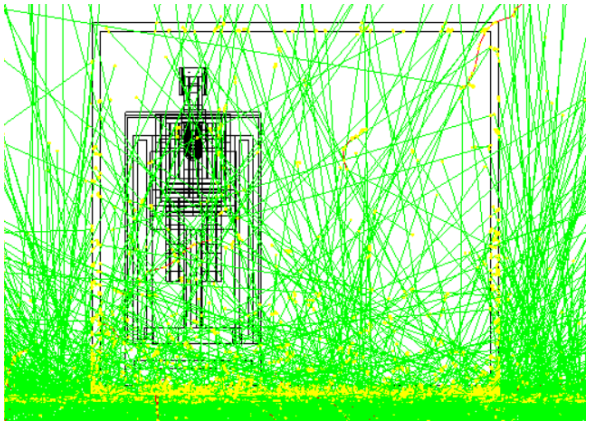

(a) Phantom P_3 in container, from the front.

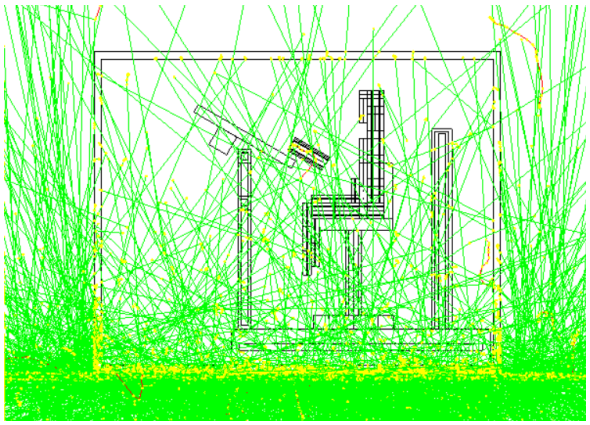

(b) Phantom P_3 in container, from the side.

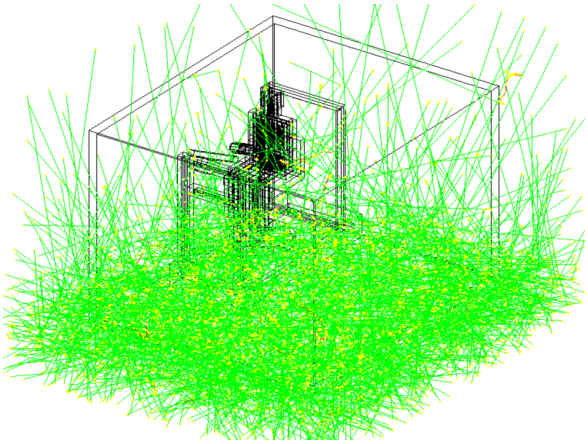

(c) Phantom P_3 in container, from an angle.

Figure 4.6: A visual aid for understanding the principle of simulate shielding done by P_3 in a radioactive contaminated area, where the first 5 cm of ground underneath and around the container emit radiation with ^{137}Cs-characteristics. Here, the visualization shows 3000 events. If all 100 million events is to be show, neither container nor phantom would be visible.

Chapter 5

Discussion

In this chapter, the results from chapter 4 are discussed. First some general comments of the methods used, and simplifications made, when modelling the geometries within Geant4. Then the simulated results will be discussed in the same order as presented in chapter 4.

In general, the simulation framework is a helpful tool for reproducing calibration results. It shows some deviations from the calibration results, which is a product of several factors. To mention some: proximity to the detector and tilt of the phantom. It is still considered to replicate the calibration setup well, giving DSA the possibility of perform further studies to improve measurement accuracy.

5.1 General comments

When building the phantoms within Geant4 all angles such as hips and knees was assumed to be 90°, as a perfect build would be. However, this is not completely correct as confirmed by Skuterud et al. (2013) and Figure 5.1, where the hip is slightly bent. How much, if any, impact this has on the measurements are unknown and should be expanded upon in the future, for example by simulate with the phantoms tilted backwards. The factor which probably have the largest impact here, are that the shoulders and head of bigger phantoms will be slightly further back than in the simulations. The analysis in section 5.4 will probably catch up some of this, as this analysis convey a function related to proximity to the detector.

Date of calibration was not mentioned in (Skuterud et al., 2013), so the date used to calculate activity of the phantoms was set to the $365/2 = 182.5 \approx 183$ day in 2012; half way through the year. At a later time, the measured values where provided, showing that the calculated activities were not deviating to much from the activity found during calibration. The largest relative difference was found in P_3, where the calculated activity was as given in Table 4.2 and measured activity was 16 811 Bq, giving a difference of about 24 Bq. Nothing here is too surprising, as ^{137}Cs have a half life of about 30.2 years.

Earlier stated, it was decided to make individual scripts for each phantom, writing the code for the phantoms to text files before read them into the code which constructed the container. Reasons being to increase readability of the code, along with easier management of which simulations to be executed. In addition it may increase the speed of the code slightly. But, given the amount of trouble this choice lead to, it is debatable whereas either of these

Figure 5.1: The smallest phantom, P_1, during calibration. Detector holder, protection wall, plateau and chair visible. Small pins holds the phantom together.

statements are true. Geant4 operates in a quite linear way, meaning that placing two object (e.g container and phantom) into the same spatial volume without having one completely enclose the other, Geant4 does not understand what happens. Thus, after debugging many problems, it was found easiest to read the files with phantom code into the container and place them along other features. Simulations where run from here. An important note is that no code creating the phantoms can overlap with features inside the container, e.g. detector stand or chair, even if it is undefined volume or just air.

Scoring is one of the most important part of the simulations, as the output data is collected here. Storing the data into several `bins`, was over all considered an interesting element, further looked upon in section 5.6. A major drawback however was deciding to letting the `bins` have 1 cm thickness. This could lead to some particles be counted several times. It was decided to use this thickness due to some error messages from Geant4, but further inspection showed that this probably rooted in another error. The scoring volume could, and should, be thinner than the 1 cm used here. This to reduce the amount of multiple counting, and give a better approximation of a detector surface.

The impact of comparing a thick and a slim scoring volume would be that as more events is registered in the simulation, more photons are likely to be counted more than once. This can be explained by purely the higher amount of photons traveling into the scoring volume,

but also that more photons are expected to travel at an angle towards it. Specially photons from higher and lower parts are expected to hit the scoring volume at an angle, and relatively higher probability to travel through several `bins`. As this is hard to measure without going into deep analysis of paths traveled by photons and performing correspondingly long simulations, it is assumed for this case that multiple counts are close to proportional to phantom size. This means that calculated geometrical differences in phantoms have integrated this factor, and thus will not perturb the conclusion of this thesis in any significant way.

5.2 Equal amount of events from each phantom

Simulating a constant amount of events for each phantom was performed as a easy way to compare results between each phantom, as the number of events registered could easily be differentiated just by inspection, as seen in Table 4.1. In the same table, the numbers used for efficiency measured by the different detectors are the average of the two different runs for each phantom given in Table 4.2 and 4.3.

Due to the difference in simulated and measured efficiency (which was expected) it was necessary to normalize, resulting in the defined κ_{dec} variable. This value should eliminate the geometrical difference of the phantoms (as simulation and calibration use the same phantom geometry), so only the detector variance, which only the measured results contain, should be remain. Thus should κ_{dec} theoretically be constant for all phantoms measured with the same detector. Shown in Figure 4.2a and 4.2b, this is not the case. However, it is still interesting that the path in said figures are alike, given that these graphs are based upon different calibrations with different detectors and supported by five simulated runs.

The same results are also found by making a κ value when reproducing of results, with graph having the same path. Here, the value of P_5 are the only value notably different. Inspecting the simulated efficiencies, $\varepsilon^s_{\text{dec}}$, in Table 4.2 and 4.3, both HPGe and NaI have three of four values which correlate well, having efficiencies of 0.0119, 0.0120 and 0.0118. The last value is an odd one out, measuring 0.0097; distinctly lower than the other. Inspecting the corresponding values for P_5 in Table 4.1, which measure between 0.0096 and 0.0098, it is clear that there are two sets of values found. The P_5 reproduction of calibrations results where simulated first, with the second run of NaI results last, then the five runs of 10 million where simulated. Thus, it is likely that the first three runs gives too high values as several improvements of code where performed during simulations. This correlate well with the fact that κ should be a constant value for each detector, as a lower $\varepsilon^s_{\text{dec}}$ for phantom P_5 gives a lower κ value, and thus gives a shape nearer the one found in Figure 4.2a and 4.2b.

Still, the shape of the curves in Figure 4.2a and 4.2b are slightly increasing, all though they theoretically should be constant. But due to the similar shape found for both detectors in all simulations, it is most likely a systematic error, or that there is something in the simulations that have not been taking into account. This could be one of the rather crude estimates regarding the container wall or material within the container, a feature not taken into account or something done during calibration which have a greater impact on the different phantoms that is not taken into consideration. Most likely it is related to the tilt of the phantoms, explained next.

Mentioned previously, it is recommended to further investigate the dependence of a tilt in the phantom. For the larger phantoms, it is expected a more backward tilted posture which

increase the distance from the head and shoulders to the detector, but are able to radiate into the detector at an larger angle.

A possible consequence of backwards tilt will effect the largest phantoms most, giving κ values largest error for these phantoms. There are two way to look at this, as $\kappa = \varepsilon^s/\varepsilon^m$; either is the simulated efficiency too high for the largest phantoms or to low for the calibrated phantoms. Counterintuitive, this should mean that the simulated setup is a more efficient geometry than the slightly backward tilted geometry. This can possibly be explained by that lower body (knees and legs) contribute more to the efficiency than the uppermost body (head and shoulder).

Figure 4.1 clearly display that larger phantoms are closer to the detector. The possibility of this to explain the non-constant κ values will be discussed in section 5.4.

Interestingly shown in Figure 4.3, the efficiency lowers between P_1 and P_4 and increases from here. Given in Table 3.1, the weight and height of the phantoms increases for the first four, while only the weight increase for the three last. Using this, two easy regression can be conducted.

Using the different weight of P_4, P_5 and P_6 and their corresponding efficiencies, a quadratic expression can be found, yielding $E(w) = -\frac{1}{5000}w(0.0045w - 1)$. Here, $E(w)$ is the efficiency as a function of weight, w. This gives a brief, and very crude, estimate of the dependency of weight to the efficiency and only fitted for persons near 170 cm height.

While the given function has an small interval of effect, demanding the measured person to have a specific height, a more complex, and maybe better, approximation can be performed using the four smallest phantoms which have both increasing weight, w, and height, h. Assuming that the weight have a linear dependency (based upon the three largest phantoms), while the height have a quadratic dependency, it is possible to find an expression on the form $E(h,w) = c_1h^2 + c_2w + c_3$, where c_i are constants. Using the `lm` function in RStudio, which calculate a fitted curve based on the preferences chosen by the user, the function $E(h,w) = -0.01095(9.0 \cdot 10^{-6}h^2 - 0.0019w - 1)$ is found. This gives a slightly more accurate estimation, while still being a rough estimate. Notably, an estimate like this does have a interval of effectiveness, as an absent of phantom, $w = 0$ and $h = 0$, yields an efficiency of 0.01095, which is wrong. This is in the extreme limit however, so within the range of average people, $E(h,w)$ should be able to give a decent approximation of the efficiency in the simulated setup.

5.3 Reproducing calibrations

As expected, the simulated efficiencies where significantly higher than those measured during calibration. The main reason for this is that the detector geometry was not implemented. This means that the simulations do not account for detector differences, such as not all hits are registered and backscattering within the detector may occur. The scoring volume registers all photons passing by, acting like a perfect detector. Clearly, this gave rise to a significantly higher amount of counts registered by the simulations.

That $\varepsilon^m_{\text{NaI}}$ was, during calibration, measured to be higher than $\varepsilon^m_{\text{HPGe}}$ may be understood in two different ways. Either the NaI detector is a better detector with higher efficiency, or a lesser detector that HGPe and measure more noise from the surroundings. Recalling sections 2.2.1 and 2.2.2, the latter is probably the case. The NaI detector is more prone to disturbances

form other radiating sources, and is thus in this setup used by DSA as a backup detector in case where problems occur with the HPGe (Skuterud et al., 2013).

Either detector used, calibrations and human measurements are performed at different locations, all of which will have some degree of radiation from the surroundings. Therefore, before each calibration sequence a notably longer measurement is performed of the background, with no phantoms in the chair. This measurement is then used to calculate the amount of background radiation that should be subtracted from a measurement as a function of time.

5.4 Shifting a phantom horizontally

A set of simulations while shifting P_1 back and forth in the seat was performed to look into the dependency of proximity to the detector. The results were more influential that expected.

Examine Figure 5.1, it is possible to see that the back of the chair is bent and thus allow for less broader phantoms to sit further back into the chair. In reality, the difference in distance is about 0 cm to 5 cm, with P_1 furthest back while P_5 and P_6 is placed nearest the detector.

Performing a linear regression of the simulated results in Figure 4.5, show that, in average, moving the phantom 1 cm horizontally will result in an increased or decreased efficiency of 0.0005. Nearer the detector gives higher efficiency.

Looking at the phantom width in Figures 3.2c, 3.3c, 3.4c, 3.5c, 3.6c and 3.7c, it increase from 220 cm to 490 cm, with the two largest phantoms having equal width. Practically this will lead to that smaller phantoms will, during calibration, measure a lower efficiency due to their placement further from the detector. Or, that the bigger phantoms measure higher efficiency due to their proximity. Meaning that the simulations should provide either too low efficiencies for small phantoms or too high for large phantoms.

This makes is possible to continue the problem found regarding κ values, where there seems to be a systematical error making κ lower for small phantoms than for larger, while they should be constant. Following the reasoning that a low κ could be caused by either a low simulated efficiency or a high calibrated value and vice versa, the proximity to the detector seems of account for some of this. Because, if the simulations setup places the large phantoms further away from the detector than calibrations, lower efficiencies is registered during simulation and thus a too high value of κ is calculated.

Phantom proximity seems to have a larger impact on the measurements than originally expected and could explain some of the error that simulations make, compared to the calibration.

It must be noted that the height of phantoms are not taken into consideration here. It will be expected for a taller phantom to move its head and feet into sections of space where radiation cannot hit the detector directly.

5.5 Shielding by each phantom in contaminated areas

To get some remotely reliable measurements, it was decided to run 100 million event from the 5 cm thick blanked underneath the container. Anything less would give results which

would not represent the shielding each phantom does. Table 4.4 shows that it is possible some draw some information, though not a conclusion, from the data. It was decided to use the total number events hitting the detector rather than the amount within the ROI area represented in *Peak*, as the values here differs too much.

Not surprisingly it was found that the largest phantoms shields largest portions of the radiation, while the smaller phantoms shields next to no radiation. Mainly this can guessed due to the pure size of phantoms. The plateau which the chair stand upon contains a core of lead, meaning that few photons are able to access the scoring volume from straight underneath. Thus, the majority of simulated hits are radiated at an angle, giving width an height of a phantom greater impact of shielding.

Again looking at Table 4.4, the fraction gives a crude estimate of the amount shielded relative to P_1. Interestingly this is close, though not accurate, to the amount estimated by DSA. Simulated results gives smaller values of shielding factor, which could either be due to low amount of events or inadequate simulation setup. In particular, material used in the constructed container walls could give rise to a significantly decrease in photon entering the container. This should be equal for all phantoms, resulting in a theoretically even decrease for all phantoms. But due to the few registered events, it is possible that the difference is emphasized. Specially notable is the fractional difference if calculate using *Peak* values; this provide no reason for conclusion.

Summarized, with the small amount of registered hits it is difficult to deduce something more than it seems probable that larger phantoms shields more background radiation that a small phantom.

An interesting set of simulations to perform would be to use the background measurements given in Skuterud et al. (2013) to quantify background radiation, and furthermore use this to calculate the amount of events corresponding to other simulation (such as the 10 million events). This would give more and better information of the shielding, where the shielded simulation could be added to their appropriate phantom, yielding a better simulation for efficiency of the detector for different sized subjects.

5.6 Inspecting detector surfaces

Previously mentioned, the scoring volume was divided into 600 `bins`; 20 azimuthal sectors, 30 radial components and only one in the $\hat{z}$ direction. Figure 5.2 displays the detector surfaces with the number of hits in each `bin`. By examine these surfaces it is possible to get information of where the photons hit the detector, possibly giving information on what differentiate the different phantoms.

First, it is important to note that the number of registered events in each `bin` is not normalized. Meaning that the `bins` closest to the center have a significantly smaller volume compared to the `bins` furthest away from the center. It thus should be no surprise that the amount of hits is correspondingly small near the center. The flux, events per volume, would be a more accurate value to use.

However, it is possible to draw some information from the detector surfaces, as the areas does not change for angular variance. The interesting part, is that the surfaces appear to have differences of where the hits are registered; top and bottom have more hits registered than the sides. First factor which contribute to this, is probably the height of the phantoms.

All phantoms are taller than they are wide, yielding a higher density of sources in the vertical direction.

For all surfaces, the sides appear to be mirroring each other, which is probably due to the symmetry found in all phantoms in the width direction. More interesting is the observations that lower part of the detector surface seems to dominate, compared to the upper part, for phantoms P_4, P_5 and P_6. Since these phantoms have same height, it cannot be this factor that differentiate them. Between said phantoms, it is the stomach that changes the most; P_4 and P_5 have identical legs and near-identical upper bodies, while P_6 has more massive legs, stomach and upper body. As the detector surfaces appear to have increasingly more hits in the upper and lower sections, it is possible that the stomach radiate more to these areas than the sides. However, it is worth noting that, by inspecting Table 4.1, these three phantoms also have increasingly values of events registered in *Peak*, so by normalizing the values, it might turn out that it is just an apparent difference.

This angular variation of hits, may be worth investigating further. As a recommendation, performing simulations with phantoms shifted sideways, would possibly give some results in this matter.

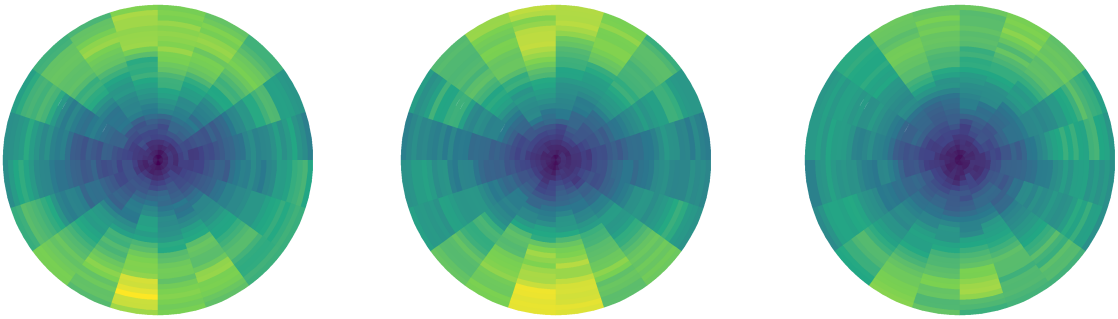

(a) Detector surface of P_1.

(b) Detector surface of P_2.

(c) Detector surface of P_3.

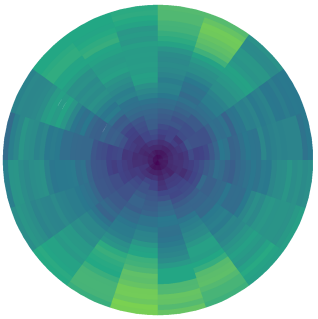

(d) Detector surface of P_4.

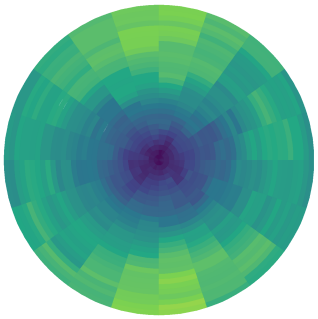

(e) Detector surface of P_5.

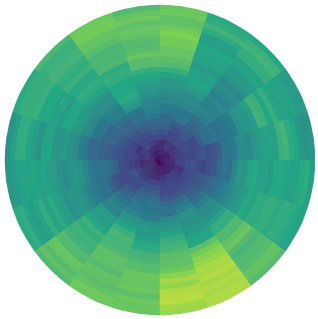

(f) Detector surface of P_6.

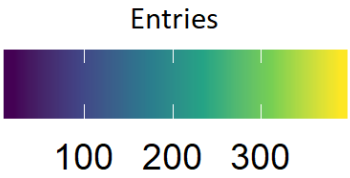

Figure 5.2: Detector surfaces of all phantoms for the first run of 10 million events. The legend are valid for all surfaces, where yellow indicated a high amount of hits, while blue few hits

Chapter 6

Conclusion

Geant4 simulation toolkit has proven to contain the needed functionality to recreate the experimental calibration setup in a simulation framework. In the implemented framework, the phantoms are been constructed in separate scripts, before they are inserted into the constructed container with the mobile laboratory. This grants the user easy access to both phantoms and container, allowing them to change any geometry. By using functions to insert each feature into the implemented world, it is easy to add or subtract features considered important for the simulations.

Through simulations, the framework has been evaluated to perform at a level that allows further usage. Some variables, such as the proximity of the person to the detector, are found to have greater impact on the measurements than expected. If the distance is decreased one cm, the efficiency is increased by up to 4.9 %, according to the simulations.

The developed framework is considered to be a viable tool for DSA to further perform simulations, in order to achieve more precise whole-body counts, compensating for human body size. DSA may alter geometries and positions variables, to examine which factors make whole-body counting most, or least, prone to inaccurate measurements. The executed simulations outline a foundation which can be further improved upon.

To continue this project, it is recommended to generate more simulations of slight variations, making it possible to understand the impact of different variables. It should in particular be looked into the effect of proximity to the detector and the potential effect of a backwards tilt of the phantoms.

Bibliography

Adams, R. A. and Essex, C. (2013). *Calculus; A Complete Course*, chapter 5, pages 311–331. Pearson Education Limited.

Agostinelli, S., J.Allison, Amako, K., Apostolakis, J., Araujoa, H., ..., Yoshida, H., and Zschiesche, D. (2003). Geant4 — a simulation toolkit. *Nuclear Instruments and Methods in Physics Research*, 506(3):250–303.
10.1016/S0168-9002(03)01368-8.

Allison, J., Amako, K., Apostolakis, J., Araujo, H., Dubois, P. A., ..., Johnson, T., and Jones, F. (2006). Geant4 developments and applications. *IEEE Transactions on Nuclear Science*, 53(1):270–278.
10.1109/TNS.2006.869826.

Allison, J., Amako, K., Apostolakis, J., Arce, P., M.Asai, ..., Yarba, J., and Yoshida, H. (2016). Recent developments in geant4. *Nuclear Instruments and Methods in Physics Research*, 835:186–225.
10.1016/j.nima.2016.06.125.

Andreo, P., Burns, D. T., Nahum, A., Seuntjens, J., and Attix, F. H. (2017). *Fundamentals of Ionizing Radiation Dosimetry*. John Wiley & Sons, Inc.

Angell, C. and Lian, B. E. (2009). *Fysiske størrelser og enheter*. Universitetsforlaget, 5th edition.

Bochud, F. O., Laedermann, J.-P., Baechler, S., Bailat, C. J., Boschung, M., Aroua, A., and Mayer, S. (2013). Monte carlo simulations of a whole-body counter using igor phantoms. *Radiation Protection Dosimetry*, 162(3):280–288.

Brookhaven National Labratory (2019). National nuclear data center.
https://www.nndc.bnl.gov/.

Direktoratet for Strålevern og Atomsikkerhet (2019a). Radioaktivitet hos reindriftsutøvere. Miljøstatus, Miljødirektoratet. Accessed 19-12-2019
https://miljostatus.miljodirektoratet.no/tema/straling/radioaktiv-forurensning/radioaktivitet-pa-land-og-i-ferskvann/radioaktivitet-hos-reindriftsutovere/.

Direktoratet for Strålevern og Atomsikkerhet (2019b). Radioaktivitet i rein. Miljøstatus, Miljødirektoratet. Accessed 19-12-2019.
https://miljostatus.miljodirektoratet.no/tema/straling/radioaktiv-forurensning/radioaktivitet-pa-land-og-i-ferskvann/radioaktivitet-i-rein/.

Eaton, D. J. and Schneider, F. (2014). *Targeted Intraoperative Radiotherapy in Oncology*, chap-

ter 5. Radiation Protection. Springer, Berlin, Heidelberg. M. Keshtgar and K. Pigott and F. Wenz (eds).

Edwards, F. and Hendee, W. (1986). Alara and an integrated approach to radiation protection. *Semin Nucl Med.*, 16(2):142–150.

Encyclopaedia Britannica (2019a). Electromagnetic spectrum. Accessed 16-10-2019 `https://www.britannica.com/science/electromagnetic-spectrum`.

Encyclopaedia Britannica (2019b). Lead. Accessed 18-10-2019 `https://www.britannica.com/science/lead-chemical-element`.

Fonseca, T. F., Bogaerts, R., Lebacq, A. L., Mihailescu, C., and Vanhavere, F. (2014). Study of the counting efficiency of a wbc setup by using a computational 3d human body library in sitting position based on polygonal mesh surfaces. *Health Physics Society*, 106(4):484–493. `0.1097/HP.0b013e3182a414ba`.

Forgan, D. (2009). *An Introduction to Monte Carlo Radiative Transfer*. Institute for Astronomy, Royal Observatory Edinburgh.

Frisvad, J. R. (2011). Importance sampling the rayleigh phase function. *Optical Society of America. Journal A: Optics, Image Science, and Vision*, 28(12):2436–2441. `10.1364/JOSAA.28.002436`.

Fukugita, M. and Yanagida, T. (2003). *Physics of Neutrinos*, chapter 3. Springer-Verlag Berlin Heidelberg.

Griffiths, D. J. (1995). *Introducttion to Quantum Mechanics*. Prentice Hall, Inc.

Hagerup-Jenssen, I. (1996). Helkroppsmåling av radioaktivitet i mennesker. *Statens StrålevernStrålevernRapport 1996: 6*, 1996(6). StrålevernRapport 1996:6.

Hall, E. J. and Giaccia, A. J. (2012). *Radiobiology for the radiologist*. Lippincott Williams and Wilkinson, a Wolters Kluwer business, 7th edition.

Harbitz, O. (2019). *Årsmelding 2018*. Direktoratet for strålevern og atomsikring.

Harrison, R. L. (2010). Introduction to monte carlo simulation. *AIP Conf Proc*, 1204:17–21. `10.1063/1.3295638`.

Helmer, R. and Chechez, V. (2017). Cs-137. Accessed 13-05-2019 `http://www.lnhb.fr/nuclides/Cs-137_tables.pdf`.

Helse- og omsorgsdepartementet (2019a). Norges lover, forskrift om strålevern og bruk av stråling , for-2016-12-16-1659. `https://lovdata.no/dokument/SF/forskrift/2016-12-16-1659?q=str%C3%A5levern`.

Helse- og omsorgsdepartementet (2019b). Norges lover, lov om strålevern og bruk av stråling, lov-2000-05-12-36. `https://lovdata.no/dokument/NL/lov/2000-05-12-36?q=str%C3%A5levern)`.

International Commission on Radiological Protection (1989). The biotogicat basis for dose timitation in the skin.

International Commission on Radiological Protection (2007). Icrp publication 103, 2007 recommendations of the international commission on radiological protection. *Ann. ICRP*, 37(2-4).

International Commission on Radiological Protection (2018). 2017 annual report. http://www.icrp.org/docs/ICRP%202017%20Annual%20Report.pdf.

International Commission on Radiological Protection, I. (1975). *Report of the Task Group on Reference Man*, volume 23. Oxford: Pergamon Press.

Kocurek, D. and Woodside, G. (1997). *Environmental, Safety, and Health Engineering*. John Wiley & Sons, Inc.

Komperød, M., Friberg, E. G., and Rudjord, A. L. (2013). Radiation doses to the norwegian population. *Statens strålevern*.

Komperød, M., Skuterud, L., and Østmo, T. (2017). Radioaktivitet i norsk mat – resultater fra overvåkningen av dyr og næringsmidler 2016. *Statens strålevern og Mattilsynet*, 10.

Kovtun, A. and Prokofyev, S. (1996). *Technical Documents of Human Whole Body Phantom with Reference Samples of Radionuclides Potassium-40, Cobalt-60 and Caesium-137*. Research Institute for Industrial and Sea Hygiene.

Krane, K. S. (1987). *Introductory Nuclear Physics*. John Wiley & Sons, Inc.

Krstic, D. and Nikezic, D. (2012). Efficiency of whole-body counter for various body size calculated by mcnp5 software. *Radiation Pretection Dosimetry*, 152(1-3):179–183. 10.1093/rpd/ncs219.

Leggett, R., Williams, L., Melo, D., and Lipsztein, J. (2003). A physiologically based biokinetic model for cesium in the human body. *Science of The Total Environment*, 317(1-3):235–255. doi:10.1016/S0048-9697(03)00333-4.

Lidén, K. and Gustafsson, M. (1967). *Radioecological Concentration Processes*, chapter Relationships and Seasonal Variations of ^{137}Cs in lichen, reindeer and man in northeren Sweden 1961-1965. Pergamon Press. Bertil Åberg and Frank P. Hungate (eds).

Lilley, J. (2001). *Nuclear Physics: principles and applications*, chapter 6, pages 151–180. John Wiley and Sons Ltd.

Mehli, H., Skuterud, L., Mosdøl, A., and Tønnessen, A. (2000). The impact of chernobyl fallout on the southern saami reindeer herders of norway in 1996. *Health Physics Society*, 79(6):683–690. 10.1093/rpd/ncs219.

Merriam-Webster's collegiate dictionary (2019). Simulation. Accessed 22-05-2019 https://www.merriam-webster.com/dictionary/simulation.

Milonni, P. W. and Eberly, J. H. (2010). *Laser Physics*. John Wiley & Sons, Incorporated. Accessed 17-10-2019.

National Aeronautics and Space Administration (NASA) (2013). The electromagnetic spectrum. Accessed 24-09-2019 https://imagine.gsfc.nasa.gov/science/toolbox/emspectrum1.html.

National Council on Radiological Protection and Measurements (2019). 2018 year in review. https://ncrponline.org/wp-content/themes/ncrp/PDFs/Annual_Rpts/2018_Annual_Rpt.pdf.

National Institutes for Quantum and Radiological Science and Technology (2019). *Basic Knowledge and Health Effects of Radiation*. Radiation Health Management Division, Ministry of the Environment, Government of Japan, 1st edition.

Schwab, M. (2011). Non-ionizing radation. In: Encyclopedia of Cancer.

Sentralbyrå, S. (2014). *Statistisk Årbok 2013*, chapter 3. Statistisk Sentralbyrå.

Singal, R. K. (2015). *Nuclear Reactor*. New Age International P Ltd., Publishers.

Skuterud, L., Dreflin, J., and Thørring, H. (2013). Stårlevernets mobile utstyr for måling av personer. *Statens strålevern*.

Skuterud, L. and Thørring, H. (2012). Averted doses to norwegian reindeer herders after the chernobyl accident. *Health Physics Society*, 102(2):208–216. 10.1097/HP.0b013e3182348e12.

Toxicology Data Network (2006). Ionizing radiation. Accessed 24-09-2019 https://toxnet.nlm.nih.gov/cgi-bin/sis/search2/r?dbs+hsdb:@term+@na+@rel+ionizing+radiation.

Wendel, C. C. (2013). *Source identification of Pu and ^{236}U deposited on Norwegian territories*. PhD thesis, Norwegian University of Life Sciences, Department of Plant and Environmental Sciences.

Wendel, C. C., Fifield, L. K., H.Oughton, D., Lind, O. C., Skipperud, L., Bartnicki, J., Tims, S. G., Høibråten, S., and Salbua, B. (2013). Long-range tropospheric transport of uranium and plutonium weapons fallout from semipalatinsk nuclear test site to norway. *Environment International*, 59.

Wood, K., Whitney, B., Bjorkman, J., and Wolf, M. (2013). *Introduction to Monte Carlo Radiation Transfer*. University of St Andrews, School of Physics and Astronomy.

Zuber, K. (2015). *Neutrino Physics*, chapter 6. Taylor & Francis Group, 2nd edition.

Appendix A

Macros

A.1 Scoring macro

```
# Scoring macro
# $ 11/2019 jonaskes@stud.ntnu.no $

# Mesh
/score/create/cylinderMesh myMesh
/score/mesh/cylinderSize 4.5 1. cm
/score/mesh/nBin 30 1 20
/score/mesh/translate/xyz -60.5 34.25 -17.7 cm
/score/mesh/rotate/rotateX 30 deg
/score/quantity/cellFlux peak
/score/filter/particleWithKineticEnergy peak 657 665 keV gamma
/score/quantity/cellFlux under
/score/filter/particleWithKineticEnergy under 0 657 keV gamma
/score/quantity/cellFlux over
/score/filter/particleWithKineticEnergy over 665 800 keV gamma
/score/close

/run/setCut 1. cm
/run/printProgress 1000
/vis/disable
/run/beamOn 10000000
/vis/enable
/vis/reviewKeptEvents

/score/drawProjection myMesh peak

/score/dumpQuantityToFile myMesh peak P1_10mil_peak_2.csv
/score/dumpQuantityToFile myMesh under P1_10mil_under_2.csv
/score/dumpQuantityToFile myMesh over P1_10mil_over_2.csv
```

```
# Confined emit volume
# $ 11/2019 jonaskes@stud.ntnu.no $
###
# source 662 keV confined to cylinders
/gps/particle gamma
/gps/pos/type Volume
/gps/pos/shape Para
/gps/pos/halfx 24.5 cm
/gps/pos/halfy 63.25 cm
/gps/pos/halfz 30.25 cm
/gps/pos/centre -60.5 20 -28.75 cm
## Radiate from ground
#/gps/pos/halfx 172.25 cm
#/gps/pos/halfy 2.5 cm
#/gps/pos/halfz 201 cm
#/gps/pos/centre 0 -112.5 0 cm
/gps/ang/type iso
/gps/energy 662 keV
/gps/source/intensity 1
/gps/pos/confine Cylinder
###
```